PONTIFÍCIA UNIVERSIDADE CATÓLICA
DO RIO DE JANEIRO

Vivian Mendes de Sousa

Pore-scale visualization and relative permeability curves of two-phase flow in fractured porous media microfluidics models.

Dissertação de Mestrado

Dissertation presented to the Programa de Pós–graduação em Engenharia Mecânica, do Departamento de Engenharia Mecânica da PUC-Rio in partial fulfillment of the requirements for the degree of Mestre em Engenharia Mecânica.

Advisor : Prof. Marcio da Silveira Carvalho
Co-advisor: Dra. Brenda Maria de Castro Costa

Rio de Janeiro
May 2025

PONTIFÍCIA UNIVERSIDADE CATÓLICA
DO RIO DE JANEIRO

Vivian Mendes de Sousa

Pore-scale visualization and relative permeability curves of two-phase flow in fractured porous media microfluidics models.

Dissertation presented to the Programa de Pós–graduação em Engenharia Mecânica da PUC-Rio in partial fulfillment of the requirements for the degree of Mestre em Engenharia Mecânica. Approved by the Examination Committee:

Prof. Marcio da Silveira Carvalho
Advisor
Departamento de Engenharia Mecânica – PUC-Rio

Dra. Brenda Maria de Castro Costa
Co-advisor
Laboratório de Microhidrodinâmica e Escoamento em Meios Porosos (LMMP) – PUC-Rio

Prof. Igor Braga de Paula
Departamento de Engenharia Mecânica – PUC-Rio

Dr. André Luiz Martins Compan
CENPES - Petrobras

Rio de Janeiro, May the 7th, 2025

All rights reserved.

Vivian Mendes de Sousa

Bachelor's degree in Petroleum Engineering from Universidade Estácio de Sá in 2015.

Bibliographic data

Sousa, Vivian Mendes de

Pore-scale visualization and relative permeability curves of two-phase flow in fractured porous media microfluidics models. / Vivian Mendes de Sousa; advisor: Marcio da Silveira Carvalho; co-advisor: Brenda Maria de Castro Costa. – 2025.

68 f: il. color. ; 30 cm

Dissertação (mestrado) - Pontifícia Universidade Católica do Rio de Janeiro, Departamento de Engenharia Mecânica, 2025.

Inclui bibliografia

1. Engenharia Mecânica – Teses. 2. Meios porosos fraturados. 3. Visualização de escoamento. 4. Escoamento bifásico. 5. Permeabilidade relativa. 6. Micromodelos. I. Carvalho, Marcio da Silveira. II. Costa, Brenda Maria de Castro. III. Pontifícia Universidade Católica do Rio de Janeiro. Departamento de Engenharia Mecânica. IV. Título.

CDD: 621

To my family.

Acknowledgments

I would like to thank God for granting me wisdom and strength during the most challenging moments of this journey. Without a doubt, His presence has guided and supported me every step of the way.

To my family, I am deeply grateful for your unconditional love, support, and encouragement. Thank you for teaching me, through your examples and dedication, the true value of hard work, ethics, and perseverance.

To my advisor, Prof. Marcio Carvalho, I am truly thankful for your guidance, patience, and the invaluable contributions that have been essential to the development of this work.

To my co-advisor, Dra. Brenda Costa, thank you for your constant support, your always relevant suggestions, and your availability throughout the entire research process. Your collaboration and encouragement have been crucial to my academic and personal growth.

To my colleagues at LMMP, I am grateful for the partnership we've built, the scientific discussions, the mutual support, and the friendships that have grown over time. The collaborative environment made this journey much easier and more fulfilling.

To my dear colleagues in the "Gray room", I am incredibly thankful for the insightful discussions, shared knowledge, and moments of relaxation. Spending time with you has been not only a source of learning but also a lot of fun. You are, without a doubt, one of the best parts of this journey.

I also thank Petrobras and CAPES for their financial support, which has been crucial for carrying out this research and for my academic development.

Finally, I want to express my gratitude to everyone who, directly or indirectly, contributed to the successful completion of this stage. To each and every one of you, a heartfelt thank you.

This study was financed in part by the Coordenação de Aperfeiçoamento de Pessoal de Nível Superior - Brasil (CAPES) - Finance Code 001.

Abstract

Sousa, Vivian Mendes de; Carvalho, Marcio da Silveira (Advisor); Costa, Brenda Maria de Castro (Co-Advisor). **Pore-scale visualization and relative permeability curves of two-phase flow in fractured porous media microfluidics models.**. Rio de Janeiro, 2025. 68p. Dissertação de Mestrado – Departamento de Engenharia Mecânica, Pontifícia Universidade Católica do Rio de Janeiro.

Multiphase flow in highly heterogeneous systems, such as naturally fractured reservoirs, plays a crucial role in oil production. In the petroleum industry, hydrocarbons extracted from these reservoirs account for a significant portion of the global oil and gas production each year. The presence of fractures, vugs, and interconnected channels in such systems introduces complexity to fluid flow either by enhancing permeability through preferential flow paths or by acting as structural barriers that restrict flow. This behavior contrasts with that of homogeneous formations and requires a deeper understanding of fluid displacement mechanisms, especially at the pore scale. Thus, the goal of this research is to investigate two-phase flow behavior in fractured porous media, focusing on the determination and analysis of relative permeability curves as a function of pore-scale phenomena. To achieve this, an experimental approach was employed, using micromodels fabricated from PDMS. These devices replicate some geometric aspects of a porous matrix composed of a random arrangement of microchannels, into which different fracture geometries were incorporated. The experimental setup enabled real-time visualization of flow dynamics and the acquisition of the data and images needed for analysis. Steady-state water-oil injection experiments were performed on both fractured and non-fractured micromodels, aiming to direct comparison the resulting relative permeability curves. The results indicate that incorporating fractures into a porous matrix alters the relative mobility of the fluid phases, and anticipates water breakthrough. These effects reduce oil displacement within the matrix and eventually lower the oil recovery. Hysteresis effects were observed during the drainage and imbibition processes, highlighting the influence of fluid saturation history on phase distribution. Moreover, distinct flow regimes were identified within the fractures as a function of the fractional flow rate of water, which affected phase interactions and, consequently, influenced the relative permeability behavior. These findings emphasize the importance of pore-scale characterization in understanding multiphase flow in fractured porous media and reinforce the potential of microfluidic as a powerful tool for analyzing transport properties in complex porous systems.

Keywords

Fractured porous media; Flow visualization; Two-phase flow; Relative permeability; Micromodels.

Resumo

Sousa, Vivian Mendes de; Carvalho, Marcio da Silveira; Costa, Brenda Maria de Castro. **Visualização em escala de poros e curvas de permeabilidade relativa do escoamento bifásico em modelos microfluídicos de meios porosos fraturados**. Rio de Janeiro, 2025. 68p. Dissertação de Mestrado – Departamento de Engenharia Mecânica, Pontifícia Universidade Católica do Rio de Janeiro.

O escoamento multifásico em sistemas altamente heterogêneos, como os reservatórios naturalmente fraturados, desempenha um papel crucial na recuperação de petróleo. Na indústria do petróleo, os hidrocarbonetos extraídos desses reservatórios representam uma parcela significativa da produção global de petróleo e gás a cada ano. A presença de fraturas, vugs e canais interconectados nesses sistemas introduz uma complexidade ao escoamento de fluidos, seja por aumentarem a permeabilidade do meio ao atuarem como caminhos preferenciais, seja por funcionarem como barreiras estruturais que restringem o escoamento. Esse comportamento contrasta com o observado em formações homogênea e exige uma compreensão mais aprofundada dos mecanismos de deslocamento de fluidos, especialmente em escala de poros. Assim, o objetivo desta pesquisa é investigar o comportamento do escoamento bifásico em meios porosos fraturados, focando na obtenção e análise de curvas de permeabilidade relativa em função dos fenômenos na escala de poros. Para isso, foi empregada uma abordagem experimental, utilizando micromodelos de meios porosos fraturados fabricados com PDMS. Esses dispositivos replicam alguns aspectos da geometria de uma matriz porosa composta por um arranjo aleatório de microcanais, nos quais foram incorporadas diferentes geometrias de fraturas. O setup experimental possibilitou a visualização em tempo real da dinâmica do escoamento e a aquisição dos dados e imagens necessárias para análise. Experimentos de injeção água–óleo em regime permanente foram realizados em micromodelos fraturados e não fraturados, com o objetivo de comparar diretamente as curvas de permeabilidade relativa obtidas. Os resultados indicam que a incorporação de fraturas em uma matriz porosa altera a mobilidade relativa das fases e antecipa a irrupção de água. Esses efeitos reduzem o deslocamento do óleo dentro da matriz e, assim, diminuem a recuperação final de óleo. Efeitos de histerese foram observados durante os processos de drenagem e embebição, evidenciando a influência da história de saturação dos fluidos na distribuição das fases. Além disso, foram identificados diferentes padrões de fluxo dentro das fraturas em função do valor do fluxo fracionário, que afetaram as interações entre as fases e, por consequência, influenciaram o comportamento das curvas de permeabilidade relativa. Esses resultados enfatizam a importância da caracterização em escala de poros para a compreensão do escoamento multifásico em meios porosos fraturados e reforçam o potencial da microfluídica como uma ferramenta poderosa para a análise de propriedades de transporte em meios porosos complexos.

Palavras-chave

Meios porosos fraturados; Visualização de escoamento; Escoamento bifásico; Permeabilidade relativa; Micromodelos.

Table of contents

1 Introduction 15
1.1 Motivation 15
1.2 Dissertation structure 17

2 Literature Review and Dissertation goals 18
2.1 Immiscible displacement in porous media 18
2.2 Experimental determination of the relative permeability in porous media 21
2.3 Microfluidic approach for pore-scale visualization 24
2.4 Numerical modeling of two-phase flow in fractured porous media 26
2.5 Research gaps 29
2.6 Dissertation goals 30

3 Materials and Methods 31
3.1 Experimental Setup 31
3.2 Working fluids and their properties 33
3.3 Porous media micromodels 33
3.3.1 Micromodels design 33
3.3.2 Mold fabrication 35
3.3.3 PDMS/glass micromodels fabrication 36
3.4 Characterization of micromodels 37
3.4.1 Dimensions, porosity and channel-size distribution 37
3.4.2 Absolute permeability measurement 38
3.4.3 Surface wettability 39
3.5 Experimental Procedure 41
3.5.1 Two-phase flow Experiments: Oil displacement by water injection 41
3.5.2 Two-phase flow Experiments: Steady-state flow with simultaneous injection of aqueous and oil phases 41
3.5.3 Two-phase flow Experiments: Relative permeability measurements 43
3.6 Image acquisition 43
3.7 Image processing 44

4 Results 46
4.1 Micromodel characterization 46
4.1.1 Characteristics of the pore space 46
4.1.2 Absolute permeability of the porous matrix 47
4.1.3 Equivalent absolute permeability of fractured micromodels 48
4.2 Evaluation of oil displacement by water injection 48
4.3 Flow regimes in fractured porous media as a function of water fractional flow 51
4.4 Analysis of oscillatory behavior at pseudo steady state 53
4.4.1 Temporal behavior of pressure drop and fluids saturation 53
4.5 Equivalent relative permeability curves of non-fractured and fractured porous media micromodels 55

4.5.1 Injection sequence I: Relative permeability curves for increasing water fractional flow rates 55
4.5.2 Injection sequence II: Relative permeability curves for decreasing water fractional flow rates 58

5 Final Remarks 60

A Appendice 67
A.1 Example of macro script used for image processing 67

List of figures

Figure 2.1 Contact between a water droplet immersed in oil and a solid surface. The contact angle is defined by the balance between the fluid-fluid interfacial tension (σ_{ow}) and the surface tensions of the oil (σ_{os}) and water phases (σ_{ws}). 19
Figure 2.2 Flow pattern diagram for drainage in homogeneous porous media, based on Lenormand (1) and Niasar and Hassanizadeh (2), showing the influence of capillary number (Ca) and viscosity ratio (M). 21
Figure 2.3 Comparison of different relative permeability curves (3). 27
Figure 2.4 Idealization of the heterogeneous porous medium as Warren and Roots (4, 5). 28

Figure 3.1 Schematic illustration of the experimental setup used in the flow tests. The apparatus is not drawn to scale. 31
Figure 3.2 Experimental setup. 32
Figure 3.3 Details of the micromodel, injection and production system, and pressure data measurement set on the inverted microscope. 32
Figure 3.4 Design of (a) porous matrix , (b) fractured Z1 , and (c) fractured L2 using CAD software. 34
Figure 3.5 Details of the pore network: on the left, an illustration of the capillary network cell demonstrates the distribution of straight and constricted channels in design. On the right is an image of the pore space of the porous matrix, with pillars illustrated in black and channels in white. 35
Figure 3.6 Scheme for obtaining microfluidic devices using the soft lithography technique. 36
Figure 3.7 Details of the fabrication process of the micromodels. 37
Figure 3.8 Graph illustrating the high-intensity peaks corresponding to the glass and PDMS surfaces in one position of the device. 38
Figure 3.9 Experimental setup to obtain absolute permeability. 39
Figure 3.10 A tile depicting the surface wettability of PDMS and glass surrounding the pore space. 39
Figure 3.11 Schematic diagram of the experimental setup for measuring contact angles using the sessile drop method. 40
Figure 3.12 Images obtained by Tensiometer for contact angle measurements showing a water droplet on PDMS and glass surfaces submerged in oil phase. 40
Figure 3.13 Experimental procedure used in the test. (a) device saturated with oil; (b) drainage with water following a protocol. 42
Figure 3.14 Experimental procedure diagram and image acquisition at each stage. (a) Mosaic merge of device saturated with oil; (b) Mosaic merge of simultaneous injection two-phase flow; (c) Tilescan acquired only in the fracture. 42

Figure 3.15 Mosaic merge of fractured L2 devices fully filled with: (a) the oleic phase, (b) the aqueous phase. 44
Figure 3.16 Illustration of the segmentation step in image processing. (a) the original image (b) image after thresholding. 44

Figure 4.1 Channel size distribution of porous matrix micromodel. 47
Figure 4.2 Measurements of pressure drop (ΔP) versus the flow rate of oil (Q_o) to obtain the absolute permeability in the porous matrix micromodel. 48
Figure 4.3 Measurements of pressure drop (ΔP) versus the flow rate of oil (Q) to obtain the equivalent absolute permeability in the fractured micromodels. 49
Figure 4.4 Porous matrix micromodels used in the tests following protocol 1, 2 and 3. Aqueous phase is in blue and oil phase is in white. 49
Figure 4.5 Water saturation (S_w) and pressure drop (ΔP) with system capillary number (Ca) variation for porous matrix device. 50
Figure 4.6 Images obtained of the fractured micromodels following protocols 1, 2, and 3 show the saturation of water and oil after the tests. The aqueous phase is in blue and the oil phase is in white. 50
Figure 4.7 Correlation of water saturation (S_w) and pressure drop (ΔP) with system capillary number (Ca) variation for Z1 fractured micromodel. 51
Figure 4.8 Images of flow structures in fractured devices. (a) occurrence of flow slugs at low water fraction flow rate (b) predominance of the stratified regime with increasing injected water flow rate. 52
Figure 4.9 Images of flow structures in Z1 fractured initially water-saturated. The stratified regime is maintained at all injection points. 53
Figure 4.10 Pressure drop (ΔP) versus porous volume (PV) after 40 PV (30 min) of simultaneous injection flow of water and oil in $f_w = 0.5$ in the porous matrix and fractured devices. 54
Figure 4.11 Pressure drop (ΔP) versus porous volume (PV) after 40 PV (30 min) of simultaneous injection flow of water and oil in $f_w = 0.5$ in the porous matrix and fractured devices. 55
Figure 4.12 Relative permeability curves obtained for the non-fractured micromodel. The curves represent the relation between water saturation (S_w) and the relative permeability of the phases (Kr_i). In this test the water fraction flow rate varying from 0.1 to 1. 56
Figure 4.13 Relative permeability curves obtained for the fractured micromodels. Water fraction flow rate varying from 0.1 to 1. 56
Figure 4.14 Relative permeability curves obtained for the non-fractured micromodel in water fraction flow rate (f_w) ranging from 1 to 0.1. 58

List of tables

Table 3.1 Properties of aqueous and oleic phases used in the experiments. 33
Table 3.2 Water flow rates injected in three different protocols presented as capillary number. 41
Table 3.3 Injected porous volume during experimental tests. 42

Table 4.1 Dimensions of the porous medium of the micromodels obtained by microscopy techniques. 46
Table 4.2 Fractured micromodel Z1 data sets obtained from relative permeability tests. 59
Table 4.3 Fractured micromodel L2 data sets obtained from relative permeability tests. 59

1
Introduction

1.1
Motivation

Multiphase flow and transport in porous media play a fundamental role in various fields of knowledge, as the ability of fluids to move through porous structures is key to many natural and industrial processes. In soil science, the flow through porous soil governs the distribution of water and nutrients, directly influencing plant growth and soil fertility. In hydrology, fluid flow through subsurface porous layers controls the recharge, storage, and preservation of groundwater resources. In chemical engineering, fluid flow in porous media enables efficient filtration and reaction processes, such as in catalyst beds. In petroleum engineering, the study of multiphase flow is crucial for assessing hydrocarbon recovery and optimizing production. Moreover, it plays a important part in addressing environmental challenges, such as enhancing techniques for carbon dioxide capture, utilization, and geological storage (CCS/CCUS) (6, 7, 8).

One of the main enhanced oil recovery (EOR) strategies currently employed in the industry is gas injection. The integration of CCS/CCUS with EOR represents a highly effective approach, in which the injection of large volumes of CO_2 not only increases the recovery of hydrocarbons but also facilitates the long-term sequestration and storage of CO_2 in geological formations (9).

The dynamics of fluids in porous media is strongly influenced by the physical characteristics of the medium. The arrangement and geometry of pores and throats governs key properties that determine fluid storage capacity and mobility (10).

In homogeneous porous media, the uniformity of the internal structure ensures that properties such as porosity and permeability remain nearly constant, minimizing variations that could affect fluid flow. In contrast, heterogeneous porous media exhibit spatial variations in geometry, leading to changes in physical properties. These formations typically consist of a homogeneous matrix of intergranular pores serving as the main storage medium, a system of macropores or vugs that are several orders of magnitude larger than the intergranular pores, and a system of fractures that may or may not be interconnected (11). When interconnected, these fractures result in an effective permeability substantially higher than the primary permeability provided by the connected pores (12) . The heterogeneity of the pore space directly influences fluid flow behavior, highlighting the need for a comprehensive understanding of the mechanisms governing multiphase flow in fractured porous media.

In the porous media analyses, Darcy equation, formulated in 1856 (13), describes the flow of incompressible fluids through a porous medium. Darcy equation defines the relationship between the flow rate through a porous medium of a fluid with known viscosity due to an imposed pressure gradient. The proportionality constant is defined as the absolute permeability of the porous medium. When multiple fluid phases are present, their flow capacity is reduced due to mutual interference. To account for this, Darcy equation is extended to include the concept of effective permeability of each phase, which varies with the phase saturation (14).

A key property for understanding and characterizing the behavior of multiphase flow is the relative permeability, which is defined as the ratio of a fluid's effective permeability to the absolute permeability of the porous medium. In practical terms, relative permeability measures how easily a fluid flows in the presence of another phase, making it a fundamental parameter for modeling and predicting flows in multiphase systems (15).

Traditionally, relative permeability is determined through standard experimental procedures using representative core plug samples. These procedures enable the analysis of fluid-rock interactions under conditions similar to those of a reservoir. Typically, these experiments involve the controlled injection of fluids through a rock sample, which is usually confined within a core holder to maintain confining pressure. Although this is the most widely used method, obtaining representative relative permeability data in a core-fluid system remains a challenging task. This method is expensive and time-consuming due to the specialized equipment required and the extended test duration. Additionally, factors such as oxidation, chemical alterations, and structural modifications in samples can influence the results. Direct visualization of fluid flow mechanisms is particularly challenging due to the opaque nature of porous media, and current images techniques can be very complex (16).

In case of heterogeneous rocks, the determination of relative permeability curves is even more challenging. The presence of vugs and fracture embedded in the porous matrix (small pores) strongly affects the flow dynamics. The configuration and geometry of fractures influence the resulting relative permeability curves. Therefore, it is important to understand the physical mechanisms by which the presence, configuration and geometry of fractures affect relative permeability curves.

In this context, microfluidic micromodels have emerged as a promising experimental approach to investigate flow in porous media. Constructed from transparent materials such as polydimethylsiloxane (PDMS) and glass, these devices enable direct visualization of flow dynamics, providing detailed insights into phase distribution. When combined with a pressure drop measurement system, microfluidic experiments allow the determination of relative permeability over time. Moreover, micromodels offer the capability to replicate complex fracture geometries and to control experimental parameters, facilitating a more in-depth analysis of phase interactions in fractured porous media.

The main goal of this study is to analyze the behavior of two-phase flow in fractured porous media by experimentally determining relative permeability curves using PDMS-based microfluidic micromodels. The results enhance understanding of flow dynamics in fractures and can lead to fundamental understanding that may improve predictive models for reservoir engineering applications.

1.2
Dissertation structure

This dissertation is structured as follows. Chapter 1 gives a brief introduction of the addressed topic and motivations and presents the scope of work. Chapter 2 presents the fundamental concepts of this work, based on a review of the previous work on experimental characterization and modeling of flows in fractured porous media. Dissertation objectives are defined in detail. Chapter 3 addresses the methodology used to carry out the experiments, a description of the experimental setup, and step-by-step experimental procedures are presented. Chapter 4 presents and discusses the results and observations regarding the characterization of the micromodels and the data obtained from the experiments. Finally, Chapter 5 displays a summary of the research conclusions, focusing on the analysis of the impact of embedded fracture in porous media, as well as recommendations for future research.

2
Literature Review and Dissertation goals

2.1
Immiscible displacement in porous media

The flow dynamics of immiscible fluids in porous media is strongly influenced by the interactions between the fluids themselves and between the fluids and the solid surfaces of the medium. Interfacial tension, wettability, viscous forces and capillary pressure are key factors that govern the distribution of fluid phases.

Interfacial tension is a thermodynamic property that describes the force per unit length acting at the interface between two immiscible phases (such as liquid-liquid or liquid-gas). It arises from molecular attractive forces, which are unbalanced at the surface or interface compared to the material's interior, leading to a higher energy state for the molecules at the interface. This imbalance causes the molecules to move toward the interior of each phase, reducing the area of the interface and minimizing the associated energy. Interfacial tension can also be understood as the energy required to increase the area of the interface between the two phases. It serves as a measure of miscibility: the lower the interfacial tension, the greater the tendency for the phases to mix (17, 18).

Wettability refers to the tendency of a fluid to adhere to or spread across the surface of a solid in the presence of another immiscible fluid. In porous media systems, for instance reservoir rocks, wettability determines which phase stays attached to the solid matrix and thus has a strong effect on two-phase flow dynamics and consequently on oil and gas recovery processes (19). Wettability is commonly quantified by the contact angle (θ), defined as the angle formed between the fluids interface with the solid surface. A contact angle less than 90° indicates that the fluid is wets the surface, while an angle greater than 90° denotes a non-wetting fluid. Angles near 0° represent strong water-wet conditions, whereas those approaching 180° suggest strong non-wetting behavior. Contact angles around 90° indicate intermediate wettability (6).

In the case of two-phase oil-water flows in porous media, wettability is fundamentally driven by the balance of interfacial forces within the oil–water–solid system. This relation is illustrated in Figure 2.1, which presents a force balance diagram described by Young's equation (20):

$$\sigma_{os} = \sigma_{ws} + \sigma_{ow} \cos\theta \tag{2-1}$$

where σ_{os} is the oil-solid surface tension, σ_{ws} is the water-solid surface tension, and σ_{ow} represents the oil-water interfacial tension. This equation characterizes the equilibrium of forces acting at the phases contact line, providing a framework for understanding wettability behavior during fluid displacement processes in porous media.

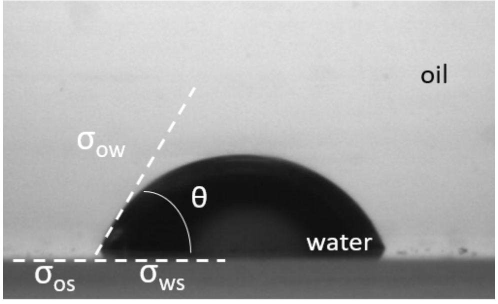

Figure 2.1: Contact between a water droplet immersed in oil and a solid surface. The contact angle is defined by the balance between the fluid-fluid interfacial tension (σ_{ow}) and the surface tensions of the oil (σ_{os}) and water phases (σ_{ws}).

Wettability has a direct impact on critical phenomena related to two-phase flow, including capillary forces, fluid saturation, and relative permeability. It is influenced by the physicochemical properties of both the fluids and the solid surface and can evolve over time due to processes such as the adsorption of compounds from the oil in the rock surface. Moreover, wettability can be spatially heterogeneous, varying across the porous medium due to differences in the mineralogical and chemical composition of a rock surface (17, 6).

Capillary pressure is defined as the pressure difference between two immiscible fluids coexisting within a porous medium. In its general form, it is expressed as $P_c = P_{nw} - P_w$, where P_{nw} is the pressure of the non-wetting phase and P_w is the pressure of the wetting phase (20). In the oil industry, capillary pressure is commonly described as $P_c = P_o - P_w$, where P_o represents the pressure of the oil phase and P_w is the pressure of the water phase. This pressure difference comes from the interfacial tension between the fluids and the curvature of their interface and is directly related to the wettability of the solid surface, which determines the shape of the meniscus at the pore scale.

The relation between capillary pressure and interface curvature is governed by the Young-Laplace equation, which in its general form is:

$$P_c = \sigma\left(\frac{1}{R_1} + \frac{1}{R_2}\right) \tag{2-2}$$

where P_c is the capillary pressure, σ is the interfacial tension between the two fluids, and R_1 and R_2 are the principal radii of curvature of the fluid interface. In the special case of cylindrical pores, the equation simplifies to:

$$P_c = \frac{2\sigma\cos\theta}{r} \tag{2-3}$$

where θ is the contact angle, and r is the radius of the pore throat. This expression indicates that capillary pressure increases as the pore throat radius decreases (20). In heterogeneous porous media, the wetting phase preferentially occupies smaller pores, while the non-wetting phase tends to fill the larger pores, influencing flow patterns and phase distribution during multiphase flow.

During imbibition process, the wetting phase displaces the non-wetting phase. In contrast, during drainage process, the non-wetting phase displaces the wetting phase, requiring higher pressure to invade narrower pore spaces (19, 21). Therefore, multiphase flow in porous media is significantly governed by the interplay between capillary and viscous forces, particularly at the pore scale. As previously discussed, capillary pressure dictates the spatial arrangement and displacement of the fluid phases within the pores and tends to dominate the flow dynamics at low flow rates. When a pressure gradient is applied, it induces viscous flow, which can alter capillary equilibrium, leading to changes in phase distribution and interface stability (11, 17).

The balance between these forces is described by the capillary number, defined as:

$$Ca = \mu v/\sigma \tag{2-4}$$

which represents the ratio of viscous to capillary forces (1). μ is the viscosity, v is the average flow velocity, and σ is the interfacial tension. Another important dimensionless parameter that governs two-phase flow in porous media is the viscosity ratio between the flowing phases, $M = \mu_d/\mu_D$, which expresses the ratio between the viscosity of the displacing fluid (μ_d) and that of the displaced fluid (μ_D)(2).

As identified by Lenormand (1) the interaction between Ca and M gives rise to three distinct flow regimes in drainage displacements in homogeneous porous media: stable displacement, capillary fingering and viscous fingering. Figure 2.2 shows a diagram of this proposed classification.

When $M > 1$ (favorable viscosity ratio), stable displacement is observed at high capillary numbers, characterized by a flat front and high sweep efficiency. However, at low capillary numbers, capillary forces dominate, leading to capillary fingering with branched and disordered invasion patterns that are

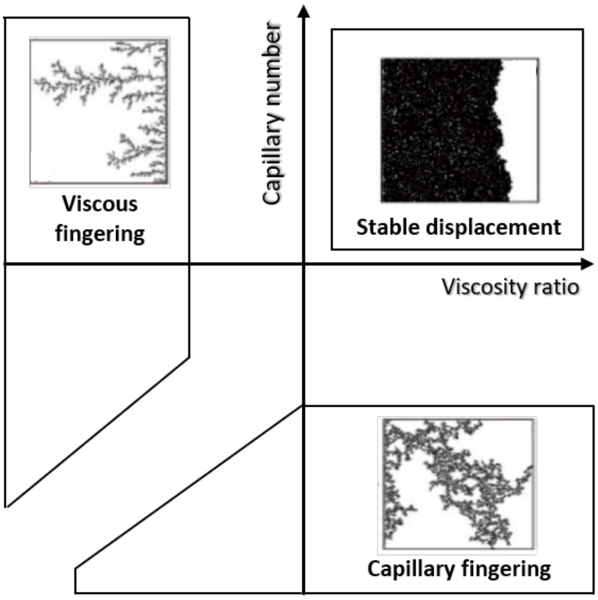

Figure 2.2: Flow pattern diagram for drainage in homogeneous porous media, based on Lenormand (1) and Niasar and Hassanizadeh (2), showing the influence of capillary number (Ca) and viscosity ratio (M).

strongly influenced by the porous structure of the medium. Conversely, when $M < 1$ (unfavorable viscosity ratio), the flow becomes dominated by viscous instabilities, resulting in viscous fingering even at high flow rates.
In this case, increasing the pressure gradient is not sufficient to stabilize the invasion front (1, 2).

2.2
Experimental determination of the relative permeability in porous media

The complex dynamics of two-phase flow through porous media is characterized by the relative permeability curves of the flowing phases. They describe how the mobility of each phase varies with the phase saturation. They are essential inputs in reservoir simulators that are commonly used to assess and predict reservoir performance (15). Therefore, accurate determination of relative permeability curves is critical for a wide range of studies focused on reservoir characterization and optimization (22).

Relative permeability data are primarily obtained through two experimental laboratory methods: steady-state and unsteady-state methods. In the steady-state method, two fluids are simultaneously injected at controlled fractional flow rates, which are maintained for extended periods to allow the system to reach steady-state, in which flow conditions stabilize. Throughout the process, key parameters such as fluids saturation, flow rates, and pressure gradients are measured. Two-phase Darcy's law is then applied to determine the effective permeability of each phase based on these measurements. By varying the fractional flow rate, relative permeability values can be obtained across different saturation levels. The collected data are then used to generate curves that illustrate the relationship between relative permeability and fluid saturation.

Steady-state methods are widely considered the most reliable and accurate for measuring relative permeability in homogeneous porous media, as they allow capillary equilibrium to be established, leading to more stable and consistent data. However, the main challenge of this method is the extended time required to reach equilibrium, which can range from several hours to days, depending on the system (23, 14).

In the unsteady-state methods, the porous medium is initially saturated with one fluid, and a displacing fluid is injected at a constant rate or pressure difference. The obtained data typically includes the total pressure difference and the production of the displaced phase a function of time. These production data are then analyzed to generate relative permeability curves using several mathematical methods, such as Welge, Johnson-Bossler-Naumann, and Jones-Roszelle, all of which are based on the Buckley-Leverett equation. Relative permeability curves can also be obtained by solving an inverse problem using flow simulators. This method generally requires less complex equipment and significantly shorter test durations than steady-state techniques (23, 14).

The use of these methods in experiments with representative core plug samples to determine relative permeability is widely documented and well established in numerous studies involving homogeneous (10, 24, 25, 26, 27) and heterogeneous porous media (28, 29, 30, 31). The following works illustrate how these methods have been adapted and interpreted in the context of fractured systems.

Rangel-German et al. (28) investigated key flow properties such as capillary pressure, relative permeability, and saturation distribution in fractured porous media through laboratory experiments and numerical simulations. Their findings highlighted the significant contribution of capillarity in flow behavior, particularly in narrow fractures where capillary continuity dominates. It was also observed that systems with wider fractures exhibited lower recovery rates, attributed to the reduced flow resistance compared to narrower fractures. Furthermore, the study emphasized the importance of accounting for heterogeneity in medium properties, such as porosity and permeability, to achieve more accurate flow predictions in simulation models.

Akin (29) conducted unsteady-state flow experiments to investigate fluid flow in fractures and the interaction between the fracture network and the surrounding matrix. The results indicated that power-law models provided a better fit for the relative permeability curves in fractures compared to linear models. Furthermore, the study concluded that dual-porosity formulations offered a more accurate representation of the underlying physical processes observed during the experiments.

Lian et al. (30) conducted steady-state flow tests on homogeneous and fractured rock samples. The results revealed marked differences in flow behavior between the two systems. In fractured media, the slope of the relative permeability curves increased, and the oil recovery factor was notably lower. This reduction in recovery is primarily attributed to the preferential flow of the injected fluid through the highly conductive fractures, which causes significant bypassing of the surrounding matrix and limits fluid displacement within it.

Vilhena et al. (31) performed an experimental and numerical investigation of spontaneous imbibition in limestone samples, both intact and fractured. Imbibition tests, micro-CT imaging, and thin-section petrography were employed to assess matrix heterogeneity and pore connectivity. Numerical simulations were calibrated to match experimental data by adjusting permeability and relative permeability properties. The results showed that stress-induced fracture deformation altered the initial fracture aperture and permeability, leading to reduced oil flow and increased fracture stiffness. These effects contributed to lower oil recovery, particularly during early production stages. The study highlights the importance of accounting for stress-driven changes in fracture aperture to improve recovery models and reservoir development strategies in fractured systems.

Although widely employed, as demonstrated in the cited studies, coreflooding experiments present several challenges and limitations. These include the extended duration required to perform the tests, and the potential for structural alterations in the samples, which compromises the reproducibility of the results. Moreover, core flooding experiments can only describe the overall behavior of the flow through the plug and cannot reveal detailed physical mechanisms in the pore scale. Even with the use of micro tomography to visualize the flow, its time and spacial resolution limits pore-scale flow visualization. To overcome some of these limitations, recent research efforts have focused on developing microfluidics systems for reservoir engineering purpose. Microfluidics allow for more controlled experiments that require much less time. It also enables pore-scale flow visualization with high time and space resolution, revealing physical mechanisms responsible for the flow dynamics.

2.3
Microfluidic approach for pore-scale visualization

With advances in experimental techniques, microfluidic micromodels have become a widely adopted and efficient tool for investigating two-phase flow in porous media. These devices, fabricated to replicate some aspects of the structure of a porous medium, are primarily used to visualize and study fluid displacement mechanisms in the pore scale during drainage and imbibition processes. The ability to observe these mechanisms at the pore scale provides valuable insight into how microscale interactions influence macroscopic flow patterns and displacement efficiency (32, 33).

Micromodels can range from simple one-dimensional (1D) configurations to more complex two-dimensional (2D) and three-dimensional (3D) geometries. In the early stages of development, transparent capillaries were employed to simulate 1D flow systems. The approach advanced using 2D models featuring parallel plates with a small gap. Subsequently, glass spheres were introduced between the plates and inside the capillaries (3D) to mimic the rock matrix and grains, with the void spaces between the spheres representing the porosity of the medium (33). These early micromodels were used not only to represent simplified porous structures but also to simulate fractures in a controlled manner, as demonstrated in several studies (34, 35, 36, 37).

The development of advanced fabrication techniques such as photolithography, etching, and molding has enabled the production of micromodels with increasingly complex and precise pore structures. These techniques allow accurate control over pore geometry, size and distribution, resulting in more realistic representations of natural porous media. Micromodels are typically constructed from transparent materials such as glass, silicon, or polymers like polydimethylsiloxane (PDMS) and polymethylmethacrylate (PMMA), which facilitate direct visualization of fluid flow at the pore scale. This capability greatly enhances the acquisition of quantitative and qualitative data related to fluid displacement mechanisms and the evolution of relative permeability over time (17).

In addition, the use of micromodels offers significant economic and operational advantages. They require smaller quantities of chemicals and energy comparing with other strategies, leading to reduced costs and lower waste generation. Their compact design occupies less physical space compared to traditional core flooding setups, and they can be operated by a single person within a shorter time frame. The relatively simple fabrication process also enhances the reproducibility of experiments. These advantages make micromodels particularly attractive for laboratory-scale investigations and support their widespread use in studies aimed at understanding the key parameters that govern flow behavior in porous media (17, 33).

Gunda et al. (16) proposed the development of a microfluidic device known as *Reservoir on a Chip* (ROC), employing advanced microfabrication techniques to replicate some aspects of the porous structure of an oil reservoir at a reduced scale. The ROC enables pore-scale displacement experiments, in which water injection is monitored to observe oil displacement dynamics. The insights gained from these experiments can be correlated with results from conventional core flooding tests, offering valuable information for understanding reservoir behavior and enhancing field-scale performance predictions.

Avendaño et al. (38) investigated the impact of surface wettability on oil displacement efficiency using glass microfluidic devices with varying channel geometries to simulate water-wet and oil-wet porous media. The study revealed that, in contrast to previous findings in natural rocks, oil-wet conditions led to more uniform displacement fronts and lower residual oil saturation, resulting in more effective oil recovery. In water-wet devices, the water invasion was more heterogeneous due to higher capillary resistance, especially in narrow pore throats, which promoted the formation of larger and more numerous oil ganglia, reducing displacement efficiency. These effects were strongly influenced by the pore geometry and low-capillary number flow conditions. The findings underscore the importance of considering wettability and pore scale geometry when evaluating multiphase flow behavior and designing enhanced oil recovery strategies.

Kenzhekhanov (39) evaluated oil displacement in NOA81 (polyester resin-based optical adhesive) micromodels with homogeneous, half-fractured, and fully fractured configurations. The results showed that oil recovery was highest in homogeneous media, while partially fractured models exhibited moderate efficiency due to partial bypassing. Fully fractured micromodels showed minimal recovery during initial water injection, as the flow concentrated in the fractures. However, extended injection improved recovery, highlighting the role of fracture connectivity in controlling displacement dynamics. Fractures acted as preferential flow paths, requiring larger injection volumes to achieve effective oil mobilization.

Hussain et al. (40) investigated two-phase flow in polyethylene and glass micromodels, as well as in limestone rock samples, to evaluate the influence of fractures and fracture inclination on fluid behavior in fractured reservoirs. The study combined flow visualization experiments, numerical validation using experimental data, and the generation of saturation profiles considering gravitational effects. The results revealed that in homogeneous models (without fractures), the displacement front advanced more uniformly, with higher mobile oil saturation. In contrast, models with fractures, especially those with a greater number of fractures, showed increased relative permeability of water and the formation of unswept zones near the fractures, leading to higher residual oil saturation. Relative permeability curves obtained both experimentally and through simulation demonstrated a nonlinear relationship between saturation and kr, reflecting the complexity of two-phase flow in oil-wet fractured media. The study highlights the need for further experimental studies to improve the understanding of two-phase flow in matrix-fracture systems with variable fracture properties.

Wu et al. (41) conducted waterflooding experiments using PDMS-based micromodels, demonstrating that wettability is a dominant factor in controlling the displacement of oil by water. Similarly, Xu et al. (42) employed PDMS devices to investigate the effects of pore geometry and interfacial tension on multiphase flow behavior. By designing geometries with identical porosities but varying configurations, they observed that both heterogeneity and pore size distribution significantly reduce oil recovery, highlighting the importance of microstructural features in displacement efficiency.

Escalante et al. (11) investigated two-phase flow in PDMS-based micromodels to evaluate how varying geometries and distributions of vugs within the porous matrix influence fluid behavior in vugular media. Their insights revealed that the presence of vugs increases the equivalent absolute permeability, promotes greater oil retention, and improves the relative permeability of water, which tends to flow preferentially through the vugular space.

To the best of our knowledge, micromodels have proven to be effective tools for reproducing complex flow patterns observed in homogeneous and heterogeneous porous media. Their ability to capture pore-scale phenomena contributes significantly to the development of more accurate and robust predictive models for flow dynamics.

2.4
Numerical modeling of two-phase flow in fractured porous media

Modeling two-phase flow in fractured media presents a significant challenge due to the complex interaction between the porous matrix and the fracture network. The presence of fractures, combined with the non-uniformity of pore geometry, affects pore connectivity, making these systems particularly difficult to model.

Various models have been developed to represent these interactions. Classical models, such as the dual-porosity model, assume that fluid flow occurs primarily through the fracture network. At the same time, the matrix acts as a secondary reservoir that exchanges fluids through capillary effects. In contrast, the dual-permeability model accounts for flow within both the matrix and the fractures, offering a more comprehensive representation of the system. Beyond these models, numerical simulations using approaches such as the multiple interacting continua (MINC) method, subdomain techniques, and discrete fracture network (DFN) models are widely employed to predict flow behavior in fractured systems (43).

Relative permeability is a fundamental parameter for estimating saturation profiles of different phases and is essential for the numerical modeling of two-phase flows. Several empirical equations are used to describe the dependence of relative permeability to phase saturation, with the most common being Corey's method.

Romm (44) conducted laboratory displacement experiments using water and kerosene between two parallel plates to estimate relative permeability of a fracture. The fracture was covered with strips and sheets of celluloid film and wax paper to divide it into several sub-fractures. As a result, the fluids flowed through many parallel channels, reducing the interaction between them. He concluded that relative permeability exhibits a linear relationship with fluid saturation ($K_{ri} = S_i$). However, these experiments neglected the effects of gravity and capillary forces. Still, Romm suggested that the linear relative permeability curve, which is represented in by × shape plot, provides an accurate representation of relative permeability in a parallel-plate fracture (45, 3, 40). Figure 2.3 presents the relative permeability curves obtained from different approaches used for modeling fluid flow in fractured media.

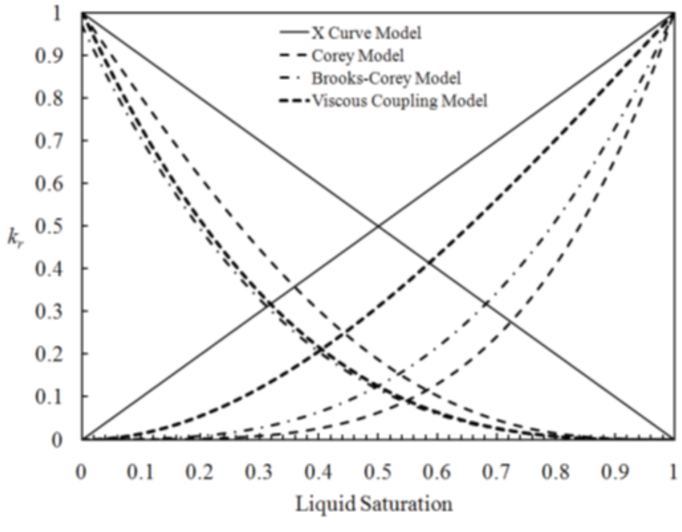

Figure 2.3: Comparison of different relative permeability curves (3).

Several studies have explored the integration of these models to describe displacement phenomena and fluid interaction in fractures and fracture-matrix systems.

Barenblatt et al. (46) established the fundamental physical principles for the mathematical modeling of fractured media, proposing a model that captures the interaction between the matrix and the fracture regions. They introduced the concept that fluid flow in fractured rock should be analyzed considering two distinct pressure components: the pressure within the fractures and the pressure within the pore space of the matrix.

Warren and Root (4) proposed that the porous system of a reservoir consists of primary porosity (intergranular) and secondary porosity (fractures and vugs). The primary porosity is composed of a set of homogeneous, isotropic, and identical rectangular blocks, which contribute significantly to the pore volume, but have minimal influence on flow capacity. In contrast, the secondary porosity is characterized by a uniform network of continuous fractures, each aligned with the principal permeability axis, providing the primary flow pathways, as show in Figure 2.4. Their model represents a superimposed arrangement of matrix and fractures, each exhibiting distinct flow regimes. The study concluded that two key properties are sufficient to describe the behavior of a dual-porosity system relative to a homogeneous porous medium: the flow capacity of the fracture network and the degree of heterogeneity within the system.

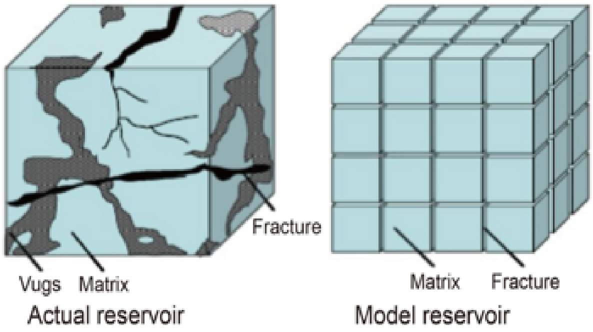

Figure 2.4: Idealization of the heterogeneous porous medium as Warren and Roots (4, 5).

Pruess and Tsang (47) developed a conceptual and numerical model for multiphase flow through rough-walled fractures. They represented fractures as two-dimensional porous media with spatially varying apertures. Their study revealed that the sum of the relative permeabilities is less than 1, the residual saturation of the non-wetting phase is significant, and phase interference is strongly influenced by the spatial correlation of fracture apertures along the flow direction.

Fourar and Lenormand (48) introduced a viscous coupling model based on the premise that the complexity of fluid interactions can be described using the theory of viscous coupling between phases. By applying this model, they successfully captured deviations of experimental data from the predictions of the linear model, highlighting the importance of viscous interactions in multiphase flow through fractures.

Watanabe et al. (49) investigated two-phase flow in fractures under several conditions of average fracture aperture, wettability, and confining stress. Their study demonstrated that for larger apertures and contact angles near 90°, relative permeabilities follow the X-curve model. However, under conditions in which capillary forces dominate, they found that Corey's method accurately describes the relative permeability curve of the wetting phase. For the non-wetting phase, they proposed a new model to capture flow behavior in capillary-dominated regimes.

Ye et al. (50) investigated the behavior of two-phase flow in rock fractures, focusing on the influence of normal deformation on flow dynamics. They developed an analytical model to predict the relationship between capillary pressure and saturation for wetting and non-wetting phases. Simulation results revealed that relative permeability is highly sensitive to the spatial correlation of fracture aperture distribution and the magnitude of the applied normal stress.

Hatami et al. (51) investigated the influence of fracture geometry and flow conditions on phase relative permeability through numerical simulations. Their results revealed that permeability is influenced by the contact area between phases, fracture morphology, and the balance between capillary and viscous forces. They observed that increasing normal stress enhances fluid interference, while higher pressure gradients promote phase segregation, bringing relative permeability curves closer to the linear model. Based on these findings, they proposed new models that demonstrated improved accuracy in predicting relative permeability compared to existing approaches.

2.5
Research gaps

Although substantial progress has been made in understanding two-phase flow in porous and fractured media, many experimental studies continue to rely on conventional rock plug techniques. While widely adopted, these methods are time-consuming, costly, and inherently limited in their ability to capture pore-scale flow phenomena due to the opacity of rock samples. In contrast, microfluidic devices have emerged as a promising partner, providing real-time visualization and precise control over experimental conditions, thereby complementing the insights obtained from rock plug studies. However, systematic studies comparing the outcomes of micromodel experiments and conventional core-based methods are still lacking. Moreover, the impact of fracture geometries on two-phase flow behavior and relative permeability remains insufficiently explored at the pore scale. This research gap highlights the need for further experimental investigations using micromodels designed to mimic fracture configurations, with the aim of elucidating how these structural features influence fluid distribution, phase interactions and recovery efficiency.

2.6
Dissertation goals

The main objective of this study is to investigate two-phase flow behavior in fractured porous media using PDMS/glass microfluidic micromodels. The study focuses on the experimental determination of relative permeability curves, quantification of fluid saturations, and the correlation between macroscopic parameters and pore-scale flow phenomena. Representative micromodels featuring artificial fractures with varying geometries are designed and fabricated. These models are integrated into a custom-built experimental setup capable of performing displacement tests under controlled flow conditions, enabling high-resolution visualization of two-phase flow and precise monitoring of pressure drop. Steady-state experiments are conducted across different fracture configurations, as well as a homogeneous porous medium reference, to evaluate the impact of fracture presence and distribution on saturation patterns, flow pathways and displacement efficiency.

3
Materials and Methods

3.1
Experimental Setup

The experimental setup was designed to capture real-time pressure drop data and images of simultaneous water-oil flow in a micromodel. Figure 3.1 presents a schematic representation of the experimental setup.

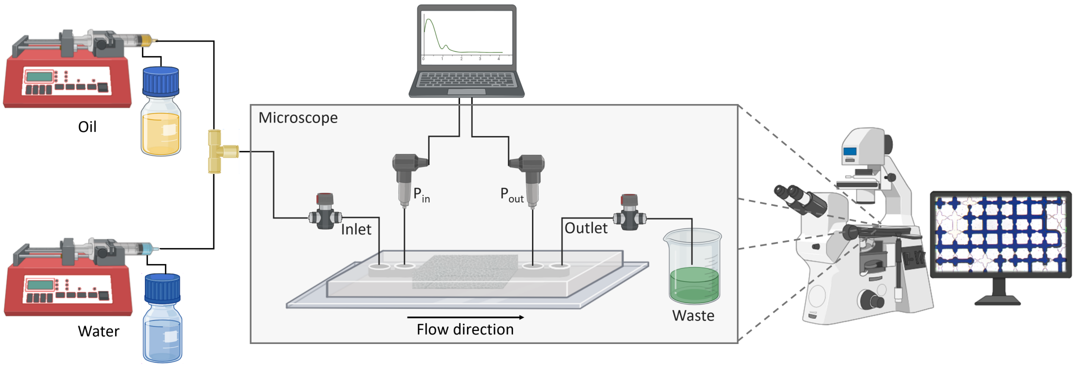

Figure 3.1: Schematic illustration of the experimental setup used in the flow tests. The apparatus is not drawn to scale.

The injection system consisted of two syringe pumps (Syringe Pump 11 Elite, Harvard Apparatus) coupled to glass syringes (1000 Series GASTIGHT, Hamilton Syringe), which were connected to the micromodel through PTFE tubing of 794 μm ID (Cole-Parmer). The flow lines were connected to a microfluidic tee connector (model P-715 from IDEX) and a four-way valve (model V-101L from IDEX), which allows the simultaneous flow of water and oil through PTFE tubing of 250 μm ID (Cole-Parmer). In the outlet port of the micromodel, a 794 μm ID tubing directs the flow produced to a waste vessel. The pressure drop (ΔP = P_i - P_o) throughout the micromodel was measured using two pressure sensors connected to the porous medium: a 15 psi transducer at the inlet port (S-10 model, WIKA) and a 1.5 psi transducer at the outlet port (S-10 model, WIKA). The sensors were connected to a computer to acquire pressure data using a universal analog input module (model NI-9203, National Instruments).

Concerning live visualization and image acquisition of the phase distribution within the porous media micromodel, a Leica DMi8 trinocular inverted microscope with motorized platinum system and digital camera (Leica MC 170-HD, Leica Microsystems) coupled to a computer was employed.

Experimental configuration is shown in figure 3.2 and details of the components that make up the apparatus are presented in figure 3.3.

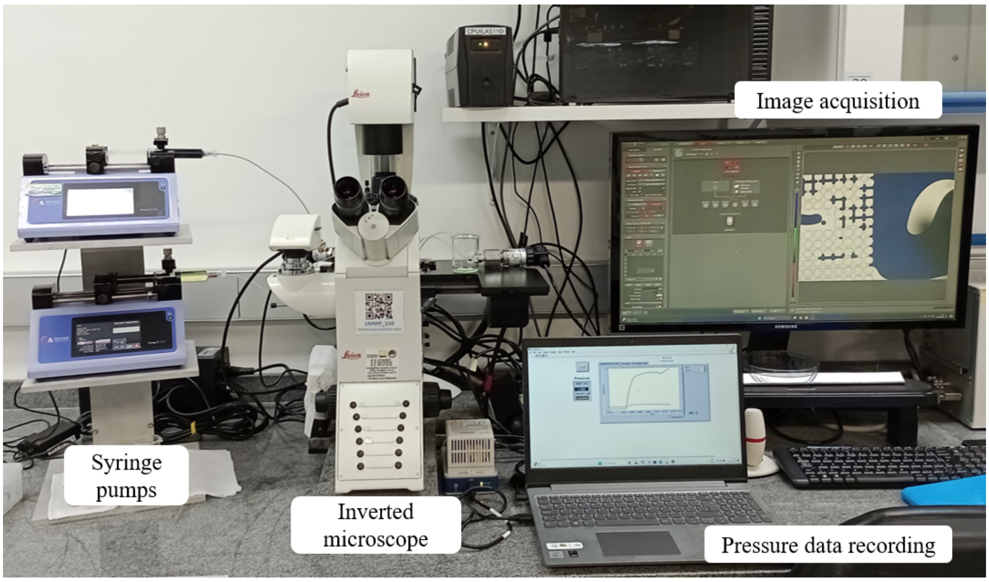

Figure 3.2: Experimental setup.

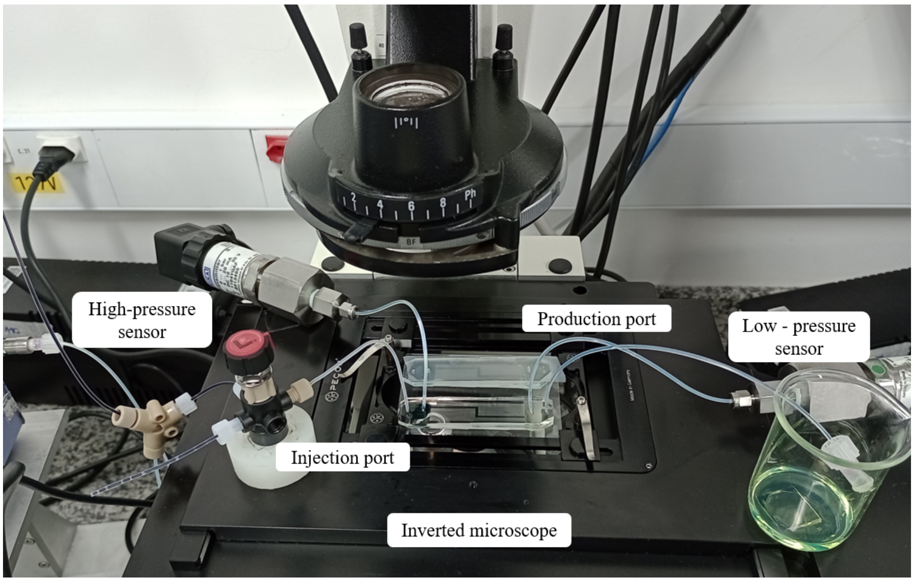

Figure 3.3: Details of the micromodel, injection and production system, and pressure data measurement set on the inverted microscope.

3.2
Working fluids and their properties

The aqueous phase used in the experiments is composed of Mili-Q® water with the addition of methylene blue (Sigma-Aldrich) at a concentration of 1.2 % w/v. The oleic phase is composed of Drakeol® 7 (Agecom) and a fluorescent dye (Oil-Glo SPI-OGG-32, Spectroline) at a concentration of 0.1 % vol. The dye was added to allow both phases to be distinguished and visualized under the microscope. Following preparation, the fluids were subjected to filtration using Millipore® membranes to remove dust and micrometer-sized particles. The aqueous phase was filtered through a 0.45 μm membrane, and the oleic phase was filtered through a 5 μm membrane.

The experiments was carried out at 22°C. The interfacial tension (σ_{wo}) between the two phases was measured with a DCAT 25 tensiometer (Data Physics Instruments) applying the Wilhelmy plate method. The dynamic viscosity was determined using a Discovery hybrid rheometer (DHR-3, TA Instrument), employing the double-walled concentric cylinder geometry, both available at LMMP/PUC-Rio.

The properties of the aqueous and oleic phases are summarized in Table 3.1.

Phases	**Components**	ρ_i (g/cm^3)	μ_i (cP)	σ_{wo} (mN/m)
Aqueous	Mili-Q® water + 1.2 % wt Methylene blue	1	0.79	8.63 ±0.02
Oleic	Drakeol® 7 + 0.1 % vol Oil-Glo	0.843	21.39	

Table 3.1: Properties of aqueous and oleic phases used in the experiments.

3.3
Porous media micromodels

Using microfabrication approach, disposable 2D micromodels were fabricated with varying configurations to emulate a porous medium. The micromodels were fabricated in a clean room facility of the Laboratory of Microhydrodynamics and Flow in Porous Media (LMMP) at PUC-Rio. Each experiment used single-use devices.

3.3.1
Micromodels design

The porous medium geometries were designed using CAD software. Figure 3.4 shows the three distinct geometries employed in this work. One configuration represents a porous medium without fractures, referred to as the porous matrix (figure 3.4.a), while the other two configurations include fractures, designated as fractured Z1 (figure 3.4.b) and fractured L2 (figure 3.4.c).

The design of the fractured porous media geometries was derived from an original layout, in which rows of pillars were removed, creating a porous medium with double porosity. The geometry of the Z1 fractured micromodel was designed by removing a single row of pillars, forming two horizontal segments connected by a vertical segment. This fracture spans the entire length of the porous medium. In contrast, the L2 fractured micromodel was constructed by removing two rows of pillars to create a single horizontal fracture. Unlike the Z1, this fracture does not extend across the entire porous medium, as it retains four vertical rows of pillars at both the inlet and outlet regions.

The micromodels have two regions, one at the inlet (injection zone) and the other at the outlet (production zone), to facilitate fluid distribution within the porous medium, ensure steady pressure at all points, and optimize the experimental procedure.

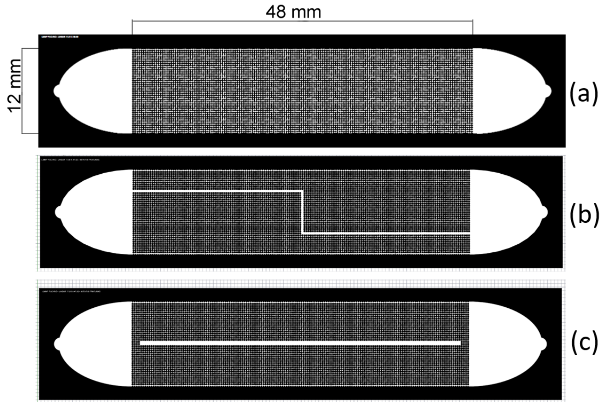

Figure 3.4: Design of (a) porous matrix , (b) fractured Z1 , and (c) fractured L2 using CAD software.

The porous matrix consists of a network of straight and constricted channels, following a pattern of 3 mm x 3 mm cells, with a network of 10 x 10 interconnected microcapillaries that repeat throughout the micromodel, resulting in a total of 6,400 capillaries. All channels have a square profile, measuring approximately 100 μm in depth and 100 μm in width, and feature randomly distributed constrictions of 50 μm (small constriction), 75 μm (large constriction), and 100 μm (straight channel) in size (figure 3.5) . The channels exhibit different throat sizes to reproduce the heterogeneity of pore throat sizes found in natural porous medium.

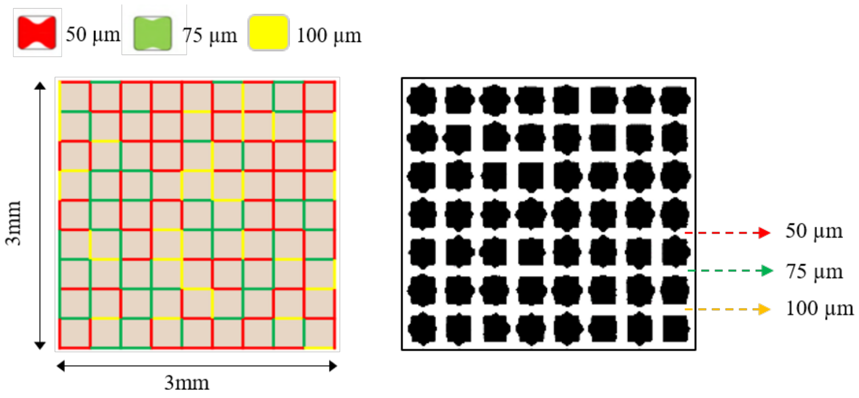

Figure 3.5: Details of the pore network: on the left, an illustration of the capillary network cell demonstrates the distribution of straight and constricted channels in design. On the right is an image of the pore space of the porous matrix, with pillars illustrated in black and channels in white.

3.3.2
Mold fabrication

The geometries of the porous media, initially designed using CAD software, were first transferred to high-resolution photomasks (3000 dpi) printed by a private company. These photomasks were then used to pattern silicon wafers (figure 3.6.a) via the soft lithography technique (52). Briefly, the silicon wafer was coated with a high-contrast, epoxy-based, negative photoresist SU-8 2025 (Kayaku Advanced Materials, USA) using a spin coating (WS-650-23B Spin Coater, Laurell Technologies, USA). Spin coating was performed in two stages: first at 500 rpm with an acceleration of 100 rpm/s for 10 seconds, followed by 1000 rpm with an acceleration of 300 rpm/s for 30 seconds. This process ensured a uniform layer of photoresist across the wafer surface, with spin speed, acceleration, and SU-8 viscosity optimized to achieve the desired layer thickness. (figure 3.6.b)

Following the coating process, the wafer underwent sequential baking steps with temperature plateaus at 65°C and 95°C to solidify and fix the photoresist. The porous medium design was transferred to the wafer by exposing the SU-8 photoresist to UV light (UV-KUB 2, Kloé, France) through the photomask. The exposure time, set at 12 seconds at 50% lamp power, was optimized based on the thickness of the photoresist layer.

After exposure, the wafer was subjected to the same baking steps and subsequently developed using propylene glycol monomethyl ether acetate (PGMEA) for 7 minutes to remove the unexposed regions of the photoresist, revealing the desired pattern. The mold was then dried using compressed air and heated at 120°C for 10 minutes to stabilize the structure, ensuring it was ready for use in micromodel fabrication. Figure 3.6 illustrates the fabrication steps for both the molds and the devices.

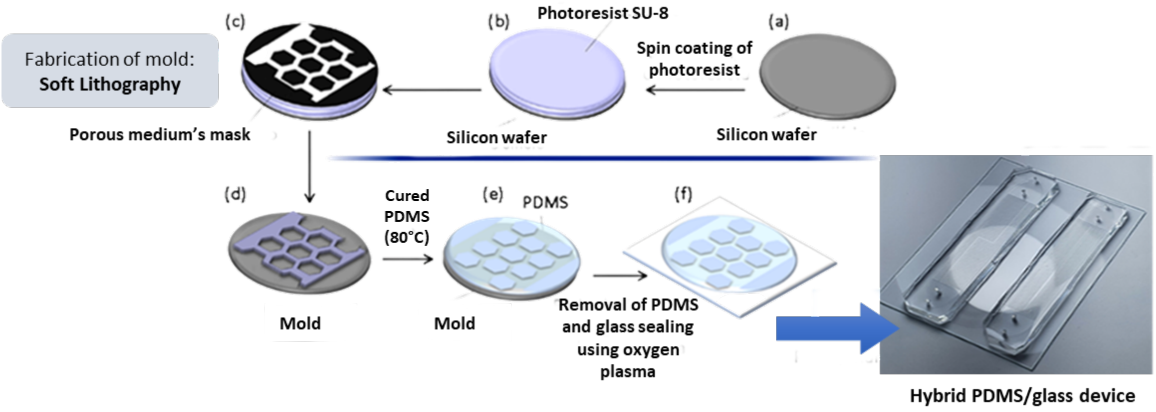

Figure 3.6: Scheme for obtaining microfluidic devices using the soft lithography technique.

3.3.3
PDMS/glass micromodels fabrication

The micromodels were fabricated using a mixture of polydimethylsiloxane (PDMS, Sylgard 184 Elastomer Kit, Dow Corning, Germany) and a reticulating agent in a 10:1 ratio. This mixture was placed under vacuum to eliminate air bubbles and then poured over the mold (figure 3.6.e). The mold containing the PDMS mixture was placed in an oven at 80°C for 2 hours to initiate polymerization and solidify the PDMS, effectively transferring the microdevice pattern from the mold to the PDMS material. Once solidified, the PDMS was carefully removed from the mold, shaped to the specified requirements, and opened at designated points to create inlet and outlet ports for fluids. Finally, the PDMS microdevice was cleaned using Scotch$^{\text{TM}}$ tape to remove any dust or dirt. Before sealing, the glass slides were washed with acetone and isopropyl alcohol and then dried with compressed air.

In the final step, the microfluidic device was sealed using a microscope glass slide to enable microscopy observations. The irreversible sealing procedure involves subjecting the device to oxygen plasma treatment (0.5 Torr, 30W) for a duration of 2 minutes. This treatment is carried out utilizing a plasma cleaner (PDC-001, Harrick Plasma, USA).

Figure 3.7 shows the path from the photomasks to the final device after bonding.

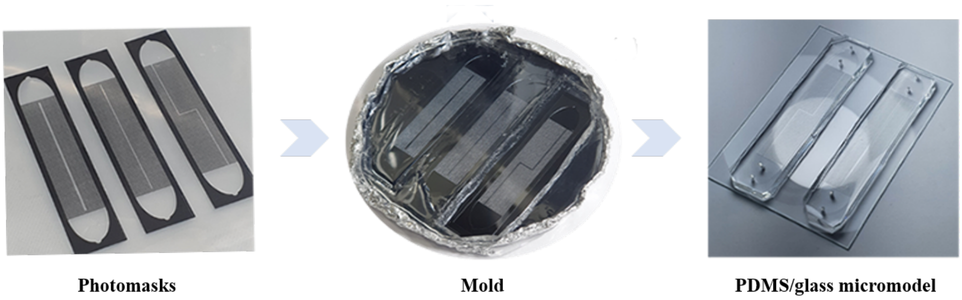

Figure 3.7: Details of the fabrication process of the micromodels.

3.4
Characterization of micromodels

This section outlines the techniques and procedures employed for the geometric and hydraulic characterization of the porous matrix and fractured porous media micromodels.

3.4.1
Dimensions, porosity and channel-size distribution

After fabrication, the geometric characterization of the micromodels was performed using optical imaging techniques, including confocal and fluorescence microscopy. Confocal laser scanning microscopy was employed to determine the height of the channels by quantifying the light reflected from the surfaces enclosing the pore space - the glass at the bottom and PDMS at the top. An optical scan along the z-axis was performed with a 638-nm laser on the air-saturated device. Due to the interaction of light with these surfaces, highly reflective areas produced peaks in light intensity as shown in Figure 3.8. By subtracting the positions of these peaks from both surfaces, the local height of each segment (tile) of the device was determined. The average channel height was calculated by aggregating the data from all tiles. This novel method, first introduced by Escalante (2023), was validated with two commercial glass micromodels, Dolomite® and Micronit®, which feature channels heights already known of 100 μm and 20 μm, respectively.

The channel size distribution and micromodel porosity were determined through image processing techniques. The devices were first saturated with an oil phase, allowing for the acquisition of high-resolution images of the porous medium. These images provided a complete view of the entire pore space, and further image processing techniques were applied to determine the areas occupied by the pores and solid pillars. Channel size distribution was measured by calculating the distances between channels. The porosity (ϕ) was determined using the Equation 3-1:

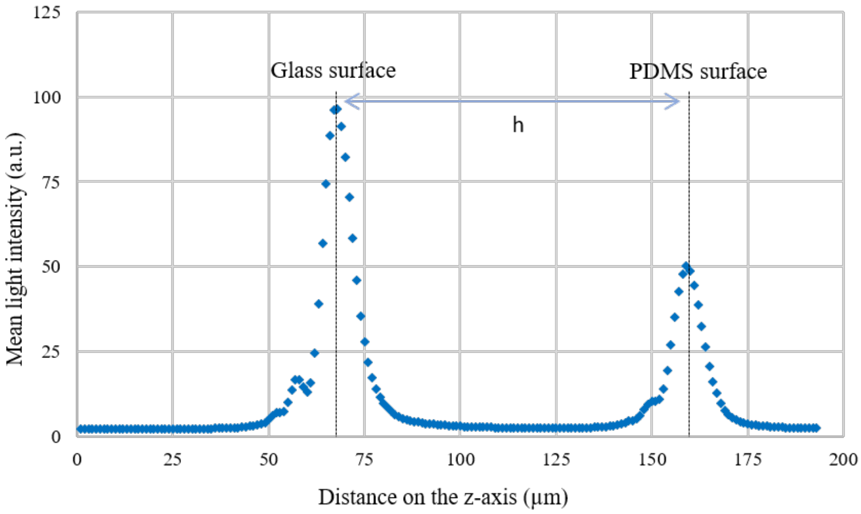

Figure 3.8: Graph illustrating the high-intensity peaks corresponding to the glass and PDMS surfaces in one position of the device.

$$\phi = \frac{A_{total} - A_{matrix}}{A_{total}} \tag{3-1}$$

where A_{total} represents the total area of the pore network and A_{matrix} represents the solid structures within the medium. The porous volume (V_{pm}) was determined by multiplying the total pore area (A_{pore}) by the average channel height (h).

3.4.2
Absolute permeability measurement

The absolute permeability (K_{abs}) of the micromodels was calculated based on single-phase Darcy's Law as Equation 3-2.

$$K_{abs} = \frac{L}{A}\mu\frac{Q}{\Delta P} \tag{3-2}$$

in which K_{abs} is the absolute permeability, L is the length of the porous medium, μ is the viscosity of the fluid, Q is the flow rate, A is the cross-sectional area of the porous medium, and ΔP is the pressure drop. The experimental setup is shown in Figure 3.9.

Initially, the devices were completely saturated with the oil solution using a single syringe pump (Harvard Apparatus Elite 11 model), coupled to glass syringe (1000 Series GASTIGHT, Hamilton Syringe) connected to the micromodel inlet port through PTFE tubing of 794 μm ID (Cole-Parmer). The pressure drop across the porous medium was measured in steady state conditions by utilizing two pressure transducers connected to the porous medium: a 15 psi transducer at the inlet (S-10 model, WIKA) and a 1.5 psi transducer at the outlet (S-10 model, WIKA) during the single-phase flow for

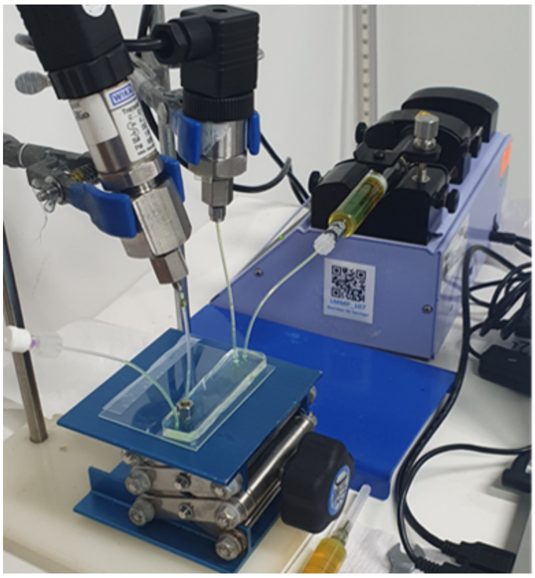

Figure 3.9: Experimental setup to obtain absolute permeability.

each flow rate injected within the range of 0.5 cc/h to 2 cc/h. The absolute permeability was calculated by fitting a linear function between the pressure drop and imposed flow rate.

3.4.3
Surface wettability

The devices exhibit hybrid wettability characteristics due to the inherent hydrophobic nature of untreated PDMS ($\theta > 90°$) and the hydrophilicity of glass ($\theta < 90°$) (53). Oxygen plasma treatment applied during the sealing process temporarily makes the PDMS walls hydrophilic, an effect that lasts for approximately 6 hours (54). The micromodels used in this study were utilized after this period to ensure they were already hybrid during the experiments, as demonstrated in Figure 3.10.

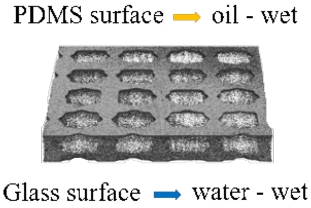

Figure 3.10: A tile depicting the surface wettability of PDMS and glass surrounding the pore space.

To evaluate the wettability of PDMS and glass with the working fluids, contact angle measurements were performed using the sessile drop method on a Standard Drop Tracker® Tensiometer (Teclis Scientific). Figure 3.11 depicts the experimental setup. The PDMS and glass surfaces were prepared following the same procedures applied during microfabrication to ensure consistent surface conditions between both materials.

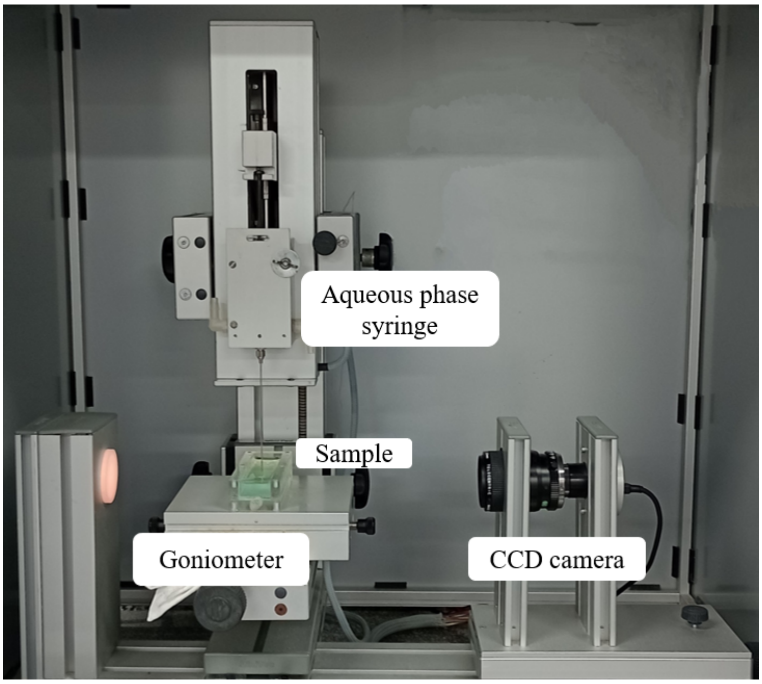

Figure 3.11: Schematic diagram of the experimental setup for measuring contact angles using the sessile drop method.

Initially, the samples were immersed in a transparent cell filled with the oleic phase. A 30 μl drop of aqueous phase was carefully placed onto the substrate using a 500 μl syringe. A CCD camera positioned in front of the goniometer captured images of the drop on the surface of the material at intervals of 0.1 seconds. The software analyzed these images and determined the contact angle based on the shape of the drop at its interface. Figure 3.12 illustrates the sessile drop method. The measured contact angle of water in the oil phase was (153.1 ± 0.8)° for PDMS and (78.9 ± 0.7)° for glass.

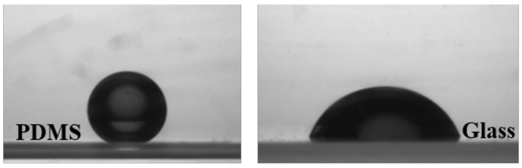

Figure 3.12: Images obtained by Tensiometer for contact angle measurements showing a water droplet on PDMS and glass surfaces submerged in oil phase.

3.5
Experimental Procedure

This section presents the experimental procedures for the three tests carried out in this work. All experiments used the same experimental setup presented in Section 3.1 and the working fluids presented in Section 3.2.

3.5.1
Two-phase flow Experiments: Oil displacement by water injection

This test was conducted to investigate the impact of varying water injection rates on oil displacement in porous matrix and Z1 fractured porous medium. Three water injection protocols were established, with an injection flow rate of 2.0 cc/h ($Ca = 4.84\times10^{-5}$) set as the upper limit, which corresponds to the working flow rate for the two-phase tests. Each protocol assumed a range of water flow rates, as shown in Table 4.1.

Q_w (cc/h)	**Protocol 1** (Ca)	**Protocol 2** (Ca)	**Protocol 3** (Ca)
0.0133	3.23×10^{-7}	3.23×10^{-7}	
0.0399	9.68×10^{-7}		
0.0667	1.61×10^{-6}		
0.1333	3.23×10^{-6}	3.23×10^{-6}	
0.667	1.61×10^{-5}		
1.333	3.23×10^{-5}	3.23×10^{-5}	
2	4.84×10^{-5}	4.84×10^{-5}	4.84×10^{-5}

Table 3.2: Water flow rates injected in three different protocols presented as capillary number.

Single-use micromodels were filled with the oleic phase at a constant flow rate of 0.5 cc/h until the porous medium was completely saturated, as illustrated in Figure 3.13.a. Throughout the experiment, the water flow rate was increased in steps according to the adopted protocol. At each step of the test, when steady-state conditions were reached (40 PV), i.e., when the pressure remained constant over time, pressure readings were recorded, and images were captured to determine the phase distributions in pore space, as shown in Figure 3.13.b.

3.5.2
Two-phase flow Experiments: Steady-state flow with simultaneous injection of aqueous and oil phases

These experiments were conducted using both the porous matrix and fractured porous medium micromodels to evaluate two characteristics of the two-phase flow:

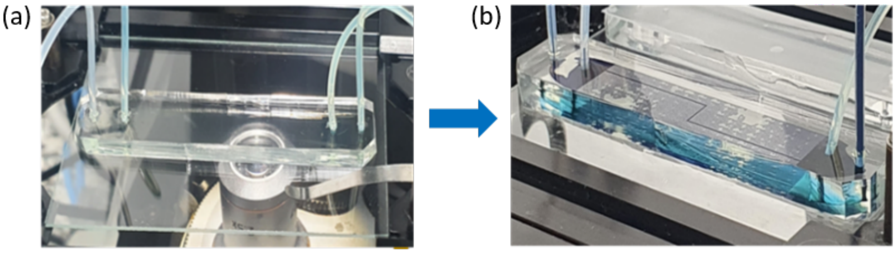

Figure 3.13: Experimental procedure used in the test. (a) device saturated with oil; (b) drainage with water following a protocol.

- ◇ the relation between pressure drop (at steady-state) and phase distribution in the pore space as a function of water fractional flow rate;
- ◇ the effectiveness of the acquired images in accurately representing the entire porous medium, including both the matrix and fractures.

Initially, the porous medium was fully saturated with the oleic phase at a constant flow rate of 0.5 cc/h. Then, water and oil were injected simultaneously at a constant total flow rate of 2.0 cc/h. The water fractional flow rate, defined as ($f_w = Q_w/Q_T$), was set to four different values, $f_w = 0.1$, 0.5, 0.9 and 1. Pressure readings were continuously recorded throughout the experiment, and at each f_w value, images of the porous medium were captured at specific time ranges corresponding to the injected pore volume determined from $V_{pinj} = Q_T \cdot t/V_{pm}$. Table 3.3 shows the time intervals used for data collection.

Injected porous volume (PV)	**time** (min)
20	15
40	30
60	45
80	60
100	80

Table 3.3: Injected porous volume during experimental tests.

Figure 3.14 illustrates the steps involved in the image acquisition process.

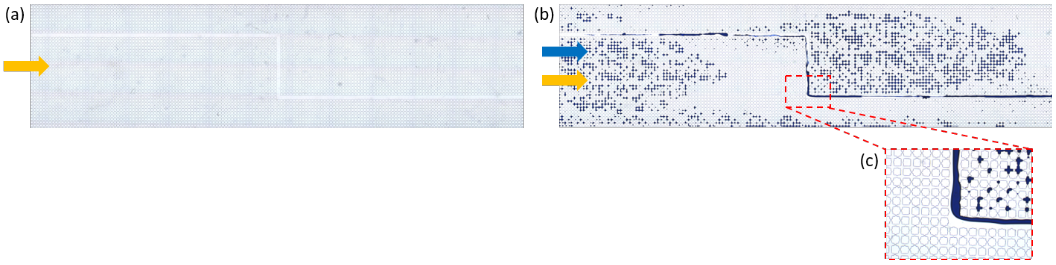

Figure 3.14: Experimental procedure diagram and image acquisition at each stage. (a) Mosaic merge of device saturated with oil; (b) Mosaic merge of simultaneous injection two-phase flow; (c) Tilescan acquired only in the fracture.

At each stage, images of the entire porous medium were acquired for both non-fractured and fractured micromodels. Additionally, in the fractured micromodels, detailed images of the flow regions inside the fractures were also captured.

3.5.3
Two-phase flow Experiments: Relative permeability measurements

Relative permeability tests were carried out to characterize the dynamic behavior of two-phase flow in fractured and non-fractured porous media. The micromodel was initially saturated with the oil phase, following the same protocol as in previous tests. After fully saturating the porous medium, the two phases were injected simultaneously at a constant total flow rate of 2 cc/h (Q_T).

During each run, the water and oil phases were injected at different values of the water fractional flow rate ($f_w = Q_w/Q_T$), ranging from 0.1 to 1 (for water-only injection). Once steady-state flow regime was achieved (after 40 PV), pressure readings and image acquisition were performed to obtain the phase distribution within the micromodel.

Using Equation 3-3, based on Darcy's law, the effective permeability (K_{eff}) of each phase was determined from the injection flow rate of the phase (Q_i) and the steady-state pressure drop (ΔP). The relative permeability was then calculated as the ratio of effective permeability to absolute permeability (K_{abs}) of the porous medium.

$$K_{eff} = \frac{L}{A}\mu_i\frac{Q_i}{\Delta P} \tag{3-3}$$

where the subscript i refers to the phase i.

3.6
Image acquisition

An inverted optical microscope, which uses visible light and optical lenses to magnify samples and generate high-resolution images, was used to capture images of the porous media through scanning techniques.

The dyes added to the fluids enhanced image contrast, with the aqueous phase, visualized in blue, being the most easily detected by the microscope. The images were acquired using a 2.5× magnification objective lens in a 2.2 MP format. Since the area of study exceeded the field of view of the objective lens, partial images (tiles) of the micromodel were captured by scanning along the x and y axes. After acquiring these tiles, a mosaic of the complete micromodel was constructed using the Leica Application Suite (LAS X), which controls both the microscope and the image capture process. The data were saved in the LIF format used in the microscope software and converted to TIFF format.

Figure 3.15 exemplifies the acquired image by the microscope of the entire pore space, after the construction of the mosaic with images of the different tiles.

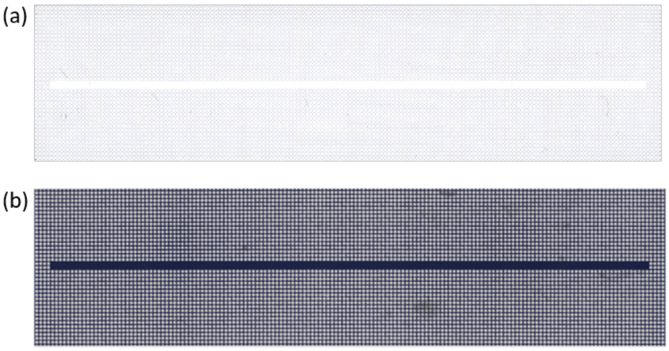

Figure 3.15: Mosaic merge of fractured L2 devices fully filled with: (a) the oleic phase, (b) the aqueous phase.

3.7
Image processing

The characterization of the pore space and quantitative measurements of the fluid saturation were obtained through digital image processing and analysis. This process involves a set of techniques applied at the pixel level to modify digital images and extract quantitative information from the samples.

The images were processed using FIJI® software, an open-source software widely used for scientific image analysis. Because a large number of images were acquired, macros were developed to automate the processing steps, ensuring consistency, reproducibility, and efficiency.

Figure 3.16 shows an example of the segmentation step of an image.

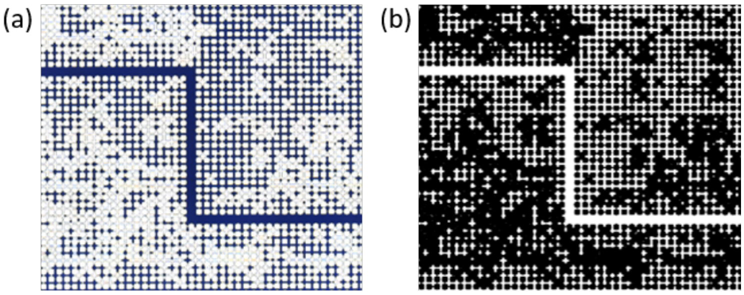

Figure 3.16: Illustration of the segmentation step in image processing. (a) the original image (b) image after thresholding.

The pre-processing included several important steps. First, images were rotated to correct any misalignment during acquisition, then flipped horizontally to standardize their orientation. A region of interest was selected by cropping the image to focus on the relevant area. Brightness and contrast were adjusted to enhance important details, and the images were converted to 8-bit format to prepare for segmentation.

Different thresholding methods were tested to optimize segmentation, with the Otsu thresholding method chosen for its effectiveness in separating regions based on pixel intensity. Segmentation was thus performed using this automatic thresholding approach, resulting in a binary image in which black and white pixels represent different areas. Post-processing steps, such as applying an outlier removal filter, were used to reduce noise and remove small residual elements, improving the quality of the segmented image.

Finally, the binary images were analyzed using the "Analyze Particles" tool to extract quantitative data like particle count and area measurements. The results were saved automatically as CSV files for further analysis. The macro scripts used for image processing followed the same general pattern but were customized for each porous medium geometry. For clarity and reproducibility, a macro script used in one of the tests was included in the Appendice as an example.

4
Results

This chapter presents the results and discussions of the geometric characterization of the PDMS/glass micromodels and the three experiments carried out to analyze the dynamics of two-phase flow in porous media with and without fractures.

4.1
Micromodel characterization

4.1.1
Characteristics of the pore space

As described in the previous chapter, the geometric characterization of the pore space was obtained using microscopy and image processing techniques.

All the micromodels fabricated had the length and width of the original design, e.g. $L = 4.8$ cm and $W = 1.18$ cm. The soft lithography process was accurate enough to produce the designed length and width of the pore space. Table 4.1 provides a summary of the measured dimensions of the different porous medium micromodels.

	Porous Matrix	**Fractured Z1**	**Fractured L2**
Height, H (μm)	91.50	89	90.60
Length, L (cm)	4.8	4.8	4.8
Width, W (cm)	1.18	1.18	1.18
Area, A (cm^2)	1.08×10^{-2}	1.05×10^{-2}	1.07×10^{-2}

Table 4.1: Dimensions of the porous medium of the micromodels obtained by microscopy techniques.

Using the dimensions of the device and data obtained from image processing, the porous volume (V_{pm}) and porosity (ϕ) of the micromodels were calculated. The following values were found, $\phi = 46\%$ for the porous matrix, $\phi = 50\%$ for the Z1 fractured model and $\phi = 50\%$ for the L2 fractured model. The pore volumes of the porous media were $V_{pm} = 23$, 24.6 and 25 μl for porous matrix, fractured Z1 and fractured L2, respectively.

As mentioned in Section 3.3.1, the porous medium constrictions were designed to be 50 μm (small constriction), 75 μm (large constriction), and 100 μm (straight channel) in width. However, due to limited resolution of the photo masks and innacuracies of the soft lithography process, a slight variation in the width of the channels occurred, as shown in Figure 4.1, which presents of throat width distributions measured. The multimodal distribution curve obtained from the measured data shows modal sizes of 29 μm, 58 μm and 87 μm for each group, respectively. Thus, despite the small difference from the original design, the same pattern of division into three groups of channels was observed.

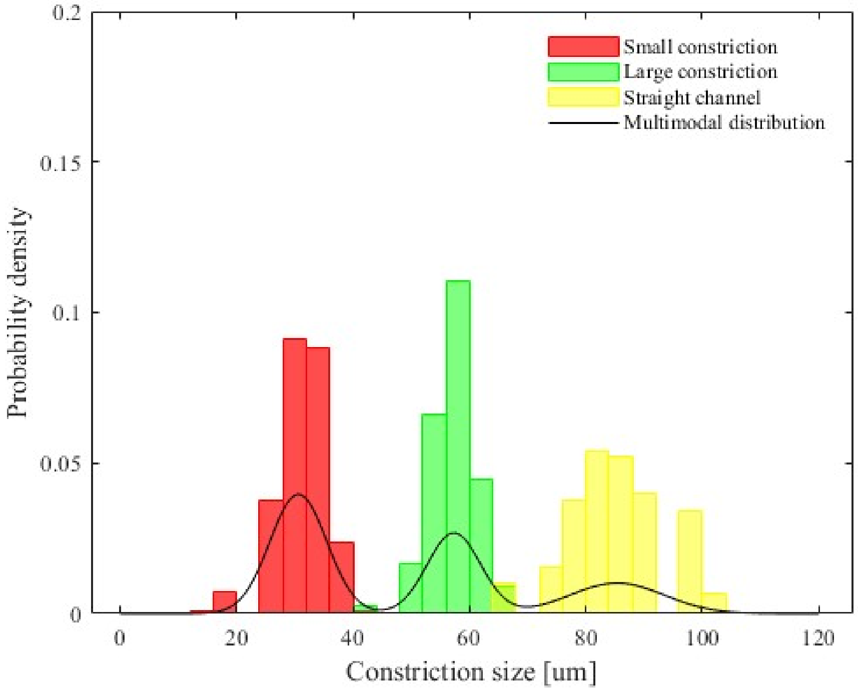

Figure 4.1: Channel size distribution of porous matrix micromodel.

Non-fractured and fractured micromodels share the porous matrix and therefore the same channel width distribution, resulting in similar constriction sizes and porosity values. This allows for a clear observation and analysis of the effect of the presence of fractures embedded in the porous matrix.

4.1.2
Absolute permeability of the porous matrix

As detailed in Section 3.4.2, the absolute permeability was determined using Darcy's law. This parameter was achieved directly from the slope of curves correlating the pressure drop with the flow rate of a single-phase fluid (oil phase in this case), taking into account the dimensions of the porous medium (Table 4.1) and the fluid viscosity (Table 3.1). The value of the porous matrix was obtained by averaging results from independent experiments, yielding K_{abs} = 25 ± 1 D. Figure 4.2 displays the resulting absolute permeability curve from a representative experiment.

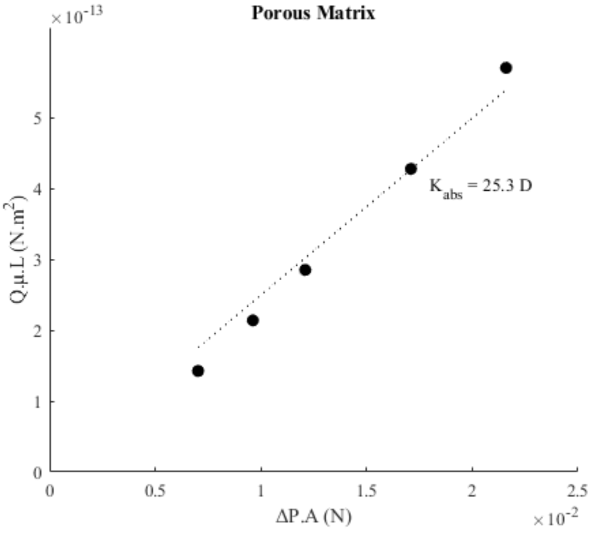

Figure 4.2: Measurements of pressure drop (ΔP) versus the flow rate of oil (Q_o) to obtain the absolute permeability in the porous matrix micromodel.

4.1.3
Equivalent absolute permeability of fractured micromodels

The equivalent absolute permeability of the fractured micromodels was determined from three measurements for each model, yielding equivalent K_{abs} $= 62 \pm 1$ D for the Z1 fractured device and $K_{abs} = 72 \pm 2$ D for the L2 fractured device. Figure 4.3 shows the pressure drop as a function of flow rate used to compute the equivalent absolute permeability of the fractured micromodels.

The presence of fractures in the porous matrix reduces pressure drop and enhances the overall capacity of the medium to conduct fluids, thus increasing the equivalent absolute permeability of the heterogeneous porous media.

4.2
Evaluation of oil displacement by water injection

In this set of experiments, the micromodel was initially fully saturated with the oil phase. The aqueous phase was injected to displace the oil phase at different total flow rates, which covered a range of capillary numbers from $Ca = 3.2 \times 10^{-7}$ to 4.8×10^{-5}, following three predefined protocols. In Protocol 1, the capillary number was varied is small steps, with five intermediate values between; in Protocol 2, the steps of variation was larger, with only 2 intermediate values; and in Protocol 3, the highest capillary number was achived in a single step. After reaching steady state in each experiment, the

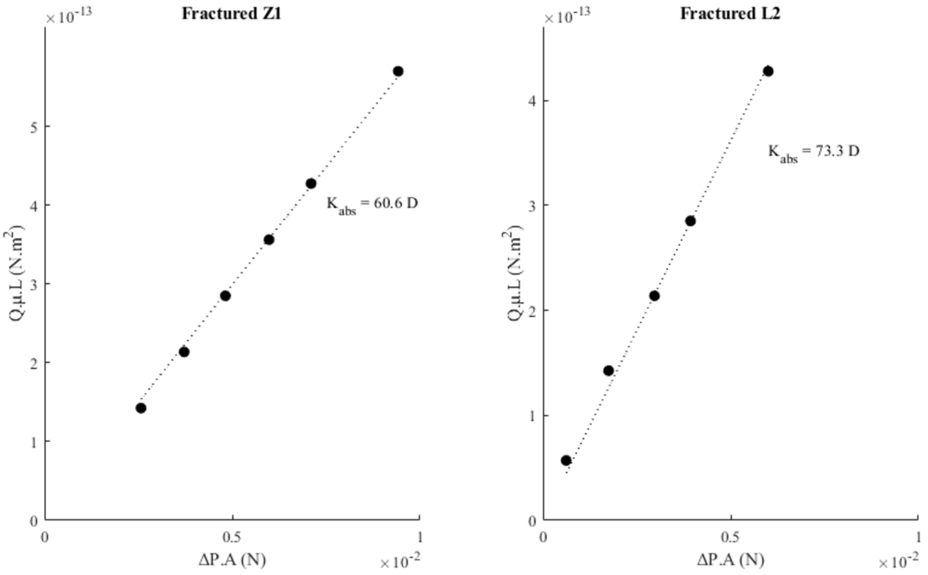

Figure 4.3: Measurements of pressure drop (ΔP) versus the flow rate of oil (Q) to obtain the equivalent absolute permeability in the fractured micromodels.

pressure difference and an image of the phase distribution in the pore space was recorded. The phase distribution at the end of each experiment are shown in Figure 4.4.

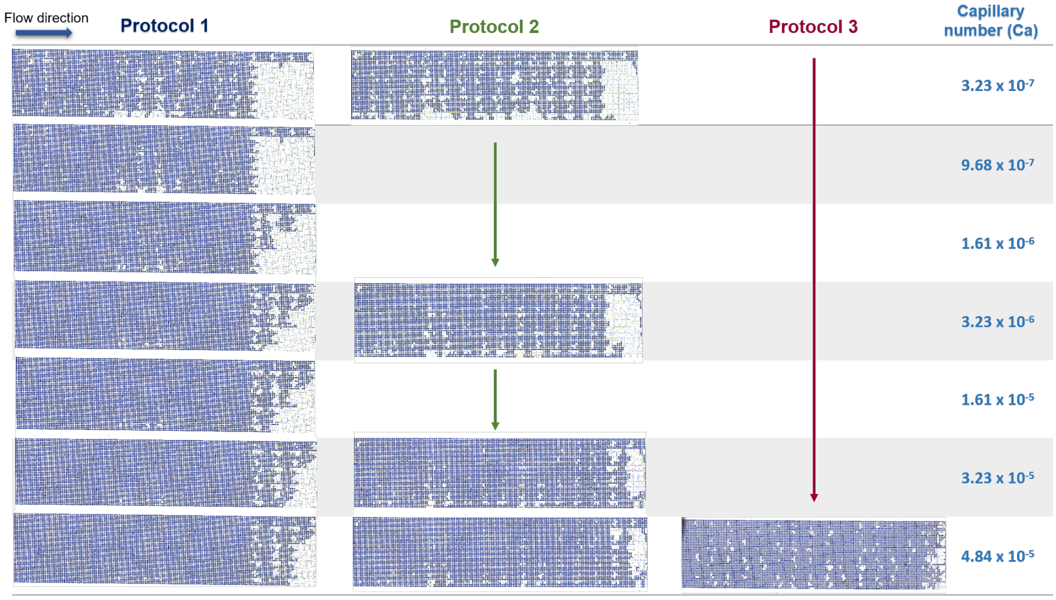

Figure 4.4: Porous matrix micromodels used in the tests following protocol 1, 2 and 3. Aqueous phase is in blue and oil phase is in white.

Figure 4.5 presents the water saturation and pressure difference as a function of capillary number for the three protocols in the porous matrix model.

The pressure difference of the flow for the different experimental protocol was approximately the same. The pressure difference is a function of capillary

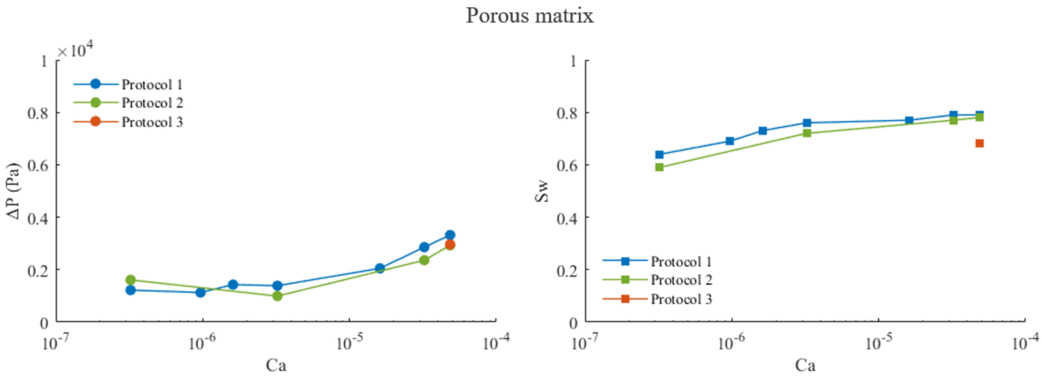

Figure 4.5: Water saturation (S_w) and pressure drop (ΔP) with system capillary number (Ca) variation for porous matrix device.

number and does not vary with the initial condition of the flow. The final water saturation, and consequently the remaining oil saturation, for protocols 1 and 2 are also approximately the same. As it expected, it rises with increasing capillary number. However, the water saturation at the highest capillary number explored obtained with protocol 3 is slightly lower than that observed with protocols 1 and 2, indicating the history of the flow may have an effect on the flow dynamics.

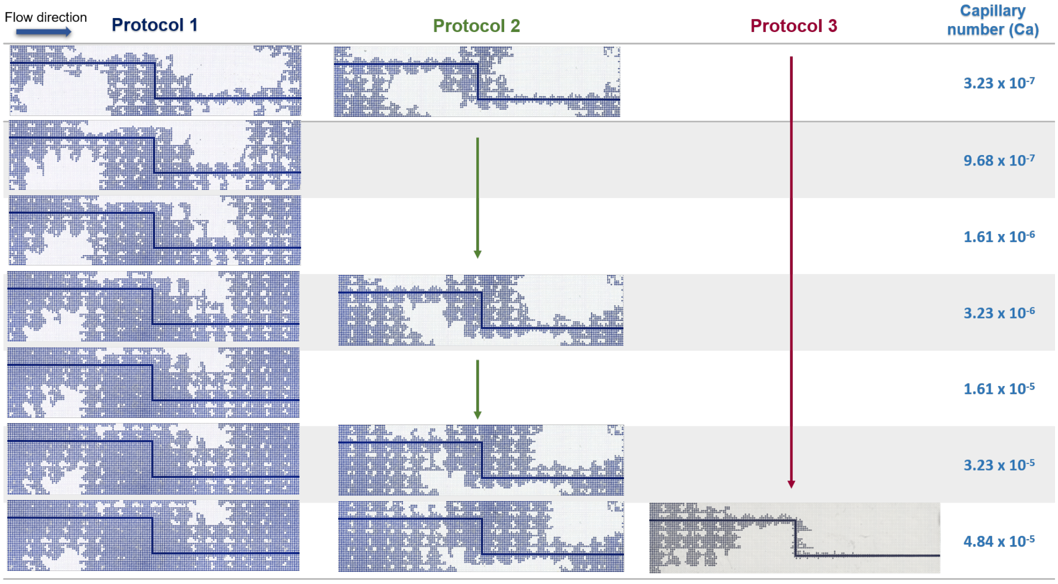

Figure 4.6: Images obtained of the fractured micromodels following protocols 1, 2, and 3 show the saturation of water and oil after the tests. The aqueous phase is in blue and the oil phase is in white.

Figure 4.6 shows the images with the phase distribution at steady state for each experiment obtained with the Z1 fractured micromodel. The impact of the initial condition on fluid behavior is clear. Unlike the porous matrix micromodel, the difference in the phase distribution at the same flow rate (capillary number) following different protocols is significant. Fig. 4.7 presents the pressure difference and water saturation at steady state as a function of capillary number for the different protocols in the fractured Z1 model. The effect of the initial condition on the pressure difference is weak. However, water saturation, and therefore remaining oil saturation, strongly varies with the experiment protocol. At a fixed capillary number, water saturation is higher with protocol 1, at which the capillary number was increased in small steps. At the lowest capillary number, e.g. $Ca = 3.23{\times}10^{-7}$, there was an 11% difference in water saturation between protocols 1 and 2, and this difference gradually increases throughout all three protocols. At the highest capillary number explored, e.g. $Ca = 4.84{\times}10^{-5}$, the difference in water saturation between protocols 1 and 2 reached 22%, while between protocols 1 and 3, it was approximately 64%.

The two-phase flow through fractured porous media shows a strong dependence on the initial condition; the phase distribution at steady state is not solely a function of the capillary number, but strongly depends on the initial condition of the phase distribution.

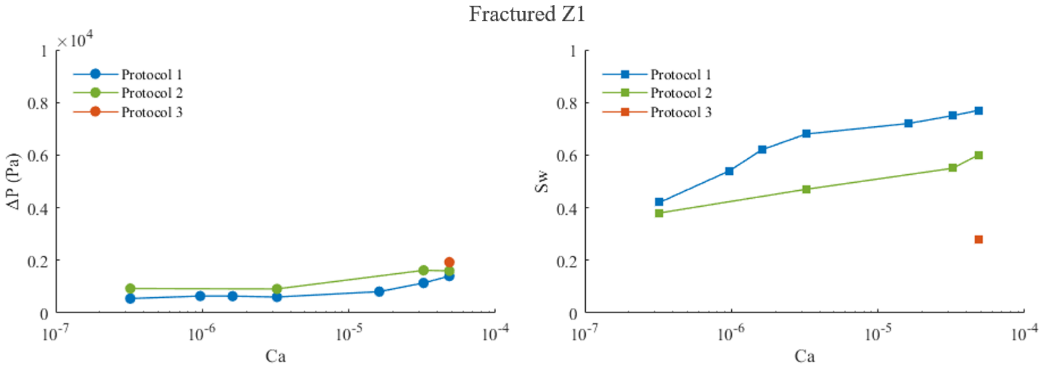

Figure 4.7: Correlation of water saturation (S_w) and pressure drop (ΔP) with system capillary number (Ca) variation for Z1 fractured micromodel.

4.3
Flow regimes in fractured porous media as a function of water fractional flow

During the two-phase flow tests in fractured porous media with simultaneous injection of both aqueous and oil phase, we observed distinct flow pattern inside the fracture depending of the water fractional flow rate. This change in flow behavior has a strong effect on the flow dynamics.

In both fractured micromodels explored, at lower water fraction flow rate values (f_w), the flow regime observed was the slug flow, characterized by water droplets moving predominantly within a continuous oil phase. In the Z1 fractured micromodel, this regime was prevalent up to $f_w = 0.3$, while in the L2 fractured micromodel, it was observed up to $f_w = 0.2$. As f_w increased beyond this point, the flow in the fractures transitioned to a stratified regime, in which the phases flowed as distinct and continuous layers. Figure 4.8 illustrates the flow regimes at various f_w values for fractured devices.

In the slug regime, both the aqueous and the oil phase move with the same velocity. The flow rate of each phase is linearly proportional to the phase saturation. In the stratified regime, the non-wetting aqueous phase moves faster, since it is lubricated by the wetting oil phase. In this case, the flow rate of each phase varies as a non-linear function of the phase saturation.

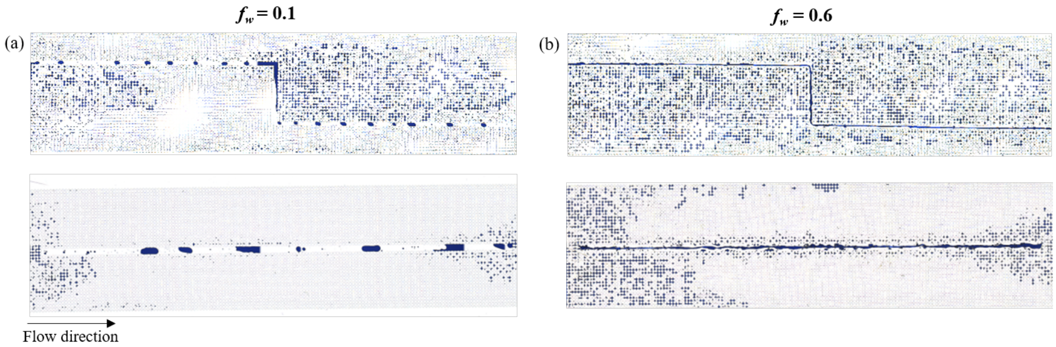

Figure 4.8: Images of flow structures in fractured devices. (a) occurrence of flow slugs at low water fraction flow rate (b) predominance of the stratified regime with increasing injected water flow rate.

This behavior can be explained by the capillary effect of two-phase flow through small channels. The micromodels used were mainly oil wet, each channel has three hydrophobic PDMS walls. Because of the hydrophobic character of the walls, the preferred flow pattern is stratified, with the wetting fluid flowing close to the walls and the non-wetting fluid flowing along the center of the channel. However, at low enough flow rate of the non-wetting aqueous phase, capillary forces destabilizes the flow, leading to the breakup of the aqueous stream into drops, leading to a slug flow pattern. There is a critical water fractional flow f_w bellow which the stratified flow is unstable.

To better understand the different flow patterns through the fracture, two-phase flow experiments were conducted using the Z1 fractured micromodel, initially saturated with the water phase. In this case, water is initially in contact in the walls and the oil phase is not able to fully displace the aqueous film attached to the wall. As shown in Figure 4.9, the change in flow regime as the fractional flow rate changes was not observed in the fracture; instead, the flow remained stratified in the range of fractional flow rate explored.

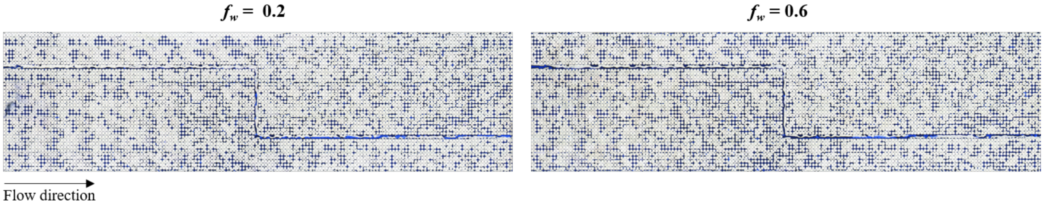

Figure 4.9: Images of flow structures in Z1 fractured initially water-saturated. The stratified regime is maintained at all injection points.

The results highlight the complexity of the two-phase flow within fractures, as will be presented in Section 4.5. The different flow regimes in the flow through the fracture has a strong effect on the behavior of the relative permeability curves.

The formation of various flow structures in fractures has also been documented in other studies (3, 55, 56). For instance, Chen et al. (55) observed flow patterns that varied based on flow rates and fluid saturation, which aligns with our observations. In both studies, the slug and droplets flow was associated with fluctuations in the flow rates, leading to complex phase movement. In contrast, stratified and channel flow developed when the flow stabilized, forming continuous channels. This comparison reinforces the idea that flow conditions play a crucial role in determining phase distribution and relative permeability trends.

4.4
Analysis of oscillatory behavior at pseudo steady state

As mentioned before, the experiments were continued until reaching steady-state conditions. In fact, the pressure difference and phase saturation actually oscillate around a time-average value, characterizing a pseudo steady-state regime. This behavior results from the intermittent dynamics of the phases as they occupy the pore space, reflecting the competition between capillary and viscous forces at the pore scale. A similar phenomenon was reported by Escalante (11) in his work on vugular porous media.

This oscillatory behavior is presented in this section. The results presented here correspond to water fractional flow rates of $f_w = 0.5$ and $f_w = 1$. Time is represented in dimensionless form as injected pore volume (PV).

4.4.1
Temporal behavior of pressure drop and fluids saturation

Figure 4.10 presents the time-evolution of pressure drop and water saturation at $f_w = 0.5$ for the porous matrix and fractured micromodels.

As shown in the pressure drop plot, after 40 PV, the time-averaged pressure difference remained constant, indicating that the pseudo steady-state condition had been reached. As expected, the pressure difference obtained with the fractured porous medium micromodels was lower than that measured in the flow through the porous matrix model.

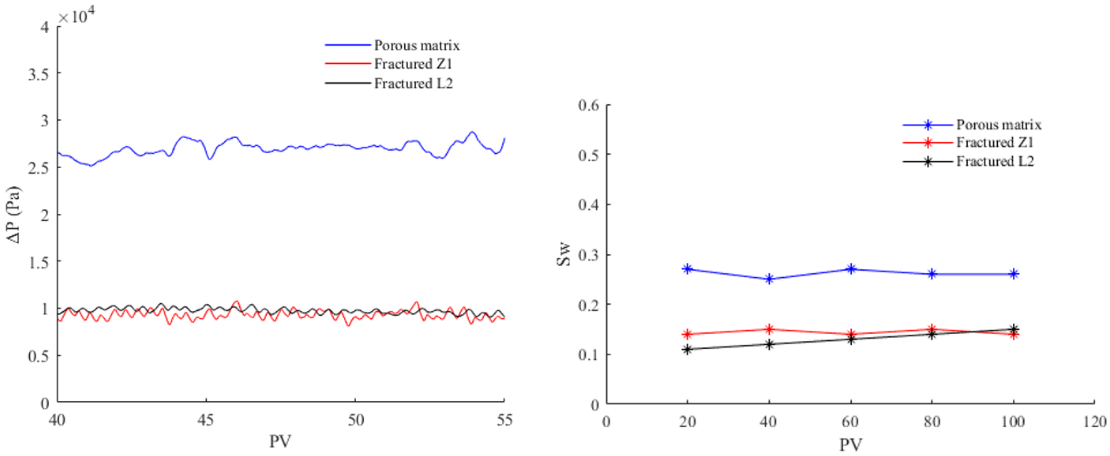

Figure 4.10: Pressure drop (ΔP) versus porous volume (PV) after 40 PV (30 min) of simultaneous injection flow of water and oil in $f_w = 0.5$ in the porous matrix and fractured devices.

Water saturation in the porous matrix and fracture Z1 micromodels is constant. For the fracture L2 model, the water saturation slowly increases with time, but the variation is very small. The measured water saturation after were $S_w = 0.26 \pm 0.007$ in the porous matrix, $S_w = 0.15 \pm 0.004$ in the Z1 fractured micromodel, and $S_w = 0.13 \pm 0.015$ in the L2 fractured micromodel. The water saturation is higher in the flow through the porous matrix micromodel. This indicates a lower oil saturation, or improved oil displacement. These results confirm that fluids saturation in the pore space remained constant after 40 PV. This behavior was consistent with the other analyzed f_w values, except for $f_w = 1$.

The time-evolution of pressure drop and water saturation at $f_w = 1$ for the porous matrix and fractured micromodels are presented in Figure 4.11.

At $f_w = 1$ (water-only injection), a more pronounced variation in fluid saturation was observed. With the three different micromodels, the water saturation slowly increases with time, even after the injection of 40 pore volumes. The porous matrix model had an average water saturation of $S_w = 0.61 \pm 0.054$, the Z1 fractured micromodel, $S_w = 0.34 \pm 0.016$, and the L2 fractured micromodel, $S_w = 0.49 \pm 0.038$. Although pressure stabilized after 40 PV, fluid saturation required much longer time to reach steady-state.

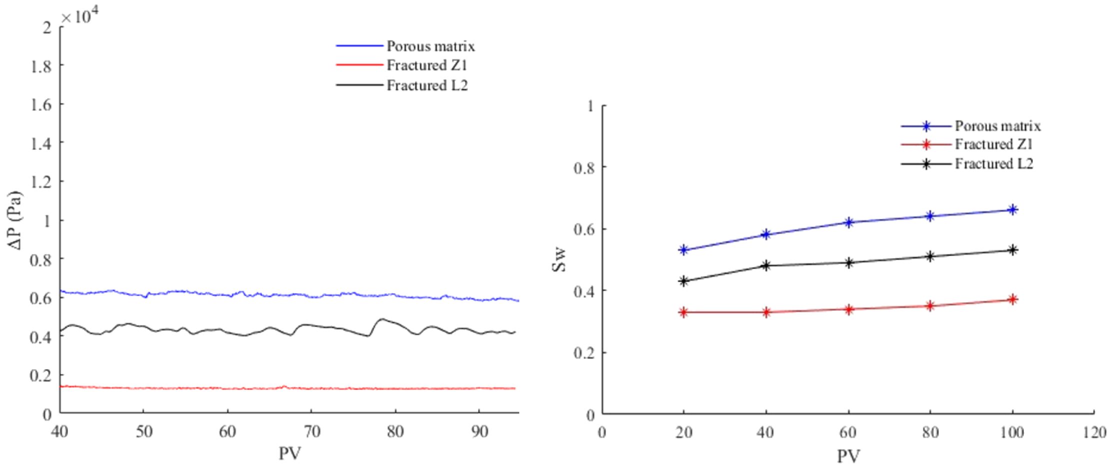

Figure 4.11: Pressure drop (ΔP) versus porous volume (PV) after 40 PV (30 min) of simultaneous injection flow of water and oil in $f_w = 0.5$ in the porous matrix and fractured devices.

Again, the water saturation was higher in the flow through the porous matrix micromodel.

To ensure standardization in obtaining pressure difference and phase saturation data in the steady-state experiments to construct the relative permeability curves, it was decided to set a limit of 40 PV for $f_w = 0.1$ to 0.9, and 80 PV for $f_w = 1$, for both the porous matrix and fractured micromodels.

4.5
Equivalent relative permeability curves of non-fractured and fractured porous media micromodels

The dynamics of two-phase flow can be characterized by the relative permeability curves of both the aqueous and oil phases. As described earlier, we experimentally obtained relative permeability curves by steady-state method for porous matrix and fractured porous media micromodels. By comparing data from micromodels with and without fractures, the impact of the presence of fractures embedded in a porous matrix can be characterized.

4.5.1
Injection sequence I: Relative permeability curves for increasing water fractional flow rates

Figure 4.12 and Figure 4.13 present the relative permeability curves of water (Kr_w) and oil (Kr_o) obtained for the porous matrix and fractured micromodels, with water fraction flow rate (f_w) varying from 0.1 to 1. Since it is not experimentally feasible to measure water saturation at $f_w = 0$ (oil-only injection), the water saturation at $f_w = 0.1$ is assumed to approximate the irreducible water saturation.

For the porous matrix micromodel, the water saturation in first point was $S_{wi} = 0.22$ and the residual oil saturation was $S_{or} = 0.46$, which corresponds to $S_w = 0.54$. The maximum value of the water relative permeability was $K_w(1 - S_{or}) = 0.12$.

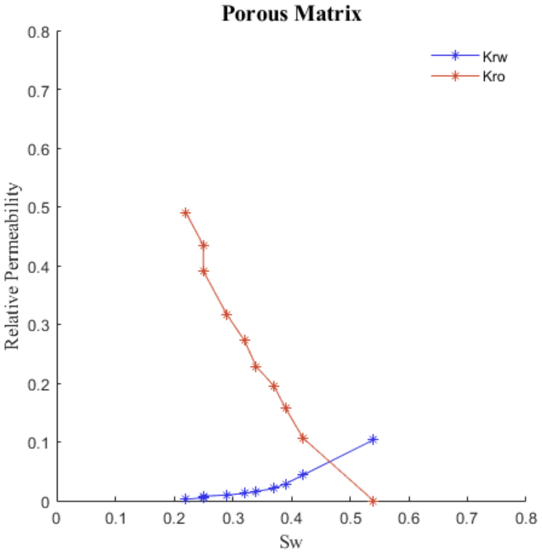

Figure 4.12: Relative permeability curves obtained for the non-fractured micromodel. The curves represent the relation between water saturation (S_w) and the relative permeability of the phases (Kr_i). In this test the water fraction flow rate varying from 0.1 to 1.

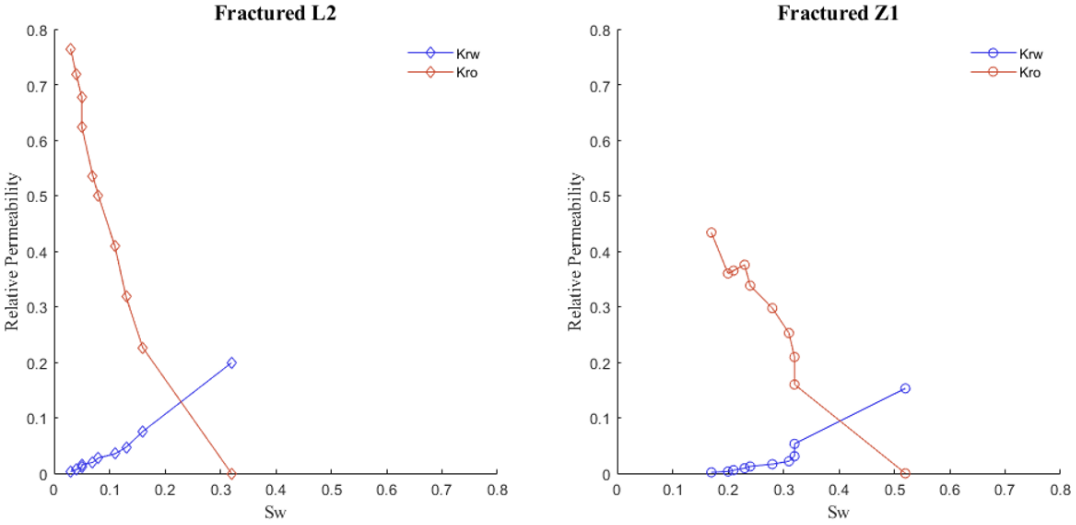

Figure 4.13: Relative permeability curves obtained for the fractured micromodels. Water fraction flow rate varying from 0.1 to 1.

The presence of fracture embedded in the porous matrix led to a decrease in the initial water saturation S_{wi}, an increase in the residual oil saturation S_{or} and an increase in the end-point of the water relative permeability curve $K_w(1 - S_{or})$. These effects are stronger in the L2 fractured micromodel. The residual oil saturation in the Z1 fractured micromodel was $S_{or} = 0.48$ and in the L2 fractured micromodel, it was $S_{or} = 0.68$. The Z1 fractured micromodel demonstrated a more effective displacement of oil by water. The narrower and more tortuous fracture channel in this geometry increased the flow resistance through the fracture. Even with the early breakthrough of water, as the water flow rate increases through the porous medium, it is forced to permeate the porous matrix, enhancing oil displacement. In contrast, the L2 fractured micromodel exhibited significantly lower fluid saturation within the porous medium. Its larger fracture channel, compared to the Z1 fractured micromodel, allowed water to percolate easily through the fracture due to its lower capillary and viscous resistance. By anticipating the breakthrough of the displacing phase, a significant number of oil ganglia remained trapped, leading to higher residual oil saturation at the end of the test ($S_{or} = 0.68$).

In fractured micromodels, a notable increase in relative permeability of water within the porous medium was observed at the final injection point (only water injection). At this stage, the fracture was fully saturated with water, as it provided the path of least resistance, allowing water to flow through it more easily. This explains the contrast with the porous matrix, in which the relative water permeability observed was lower.

As mentioned in Section 4.3, the flow regimes observed in the fractured micromodels significantly influence the behavior of the relative permeability curves. The flow structures in both fractured micromodels followed a similar pattern, with the slug flow occurring at low f_w (low S_w) and transitioning to stratified flow as f_w increases (high S_w).

The slug flow regime leads to relative low water permeability, since both aqueous and oil phases flow through the fracture with the same velocity. As the flow transitions to the stratified regime, the water permeability rises. This is clear in the plots, at which a sudden increase in water permeability with water saturation can be observed.

The analysis of relative permeability curves revealed that fractures in the porous medium led to an earlier water breakthrough, reducing oil displacement within the porous matrix and consequently decreasing oil recovery. Variations in fracture configurations significantly affected the distribution of water and oil within the porous matrix and fluids flow dynamics, both in comparison to non-fractured media and among different fractured micromodels. This highlights the critical role of fracture characteristics, such as orientation and geometry, in shaping fluid behavior within a porous medium (3).

4.5.2
Injection sequence II: Relative permeability curves for decreasing water fractional flow rates

The direction at which the phases saturation change, i.e. if it is either a drainage or imbibition process, may affect the interaction between the flowing phases and therefore the flow dynamics. At a given saturation value, different fluid distribution in the pore space may occur, leading to variations in the shape of the relative permeability curves for each process.

Figure 4.14 illustrates the relative permeability curves for water and oil in the porous matrix micromodel during decrease water fraction flow rate process, at which the water fraction flow rate (f_w) decreases from 1 to 0.1.

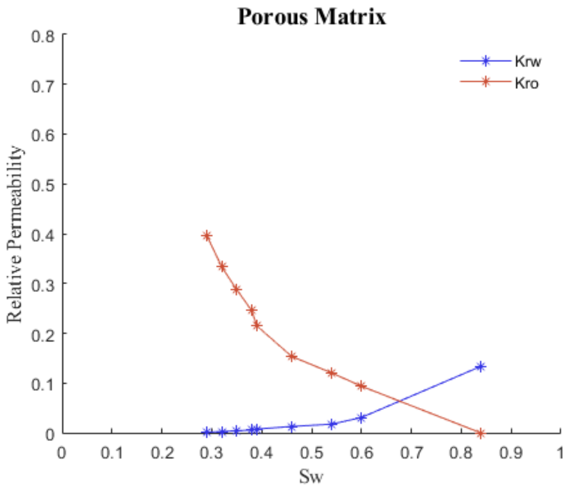

Figure 4.14: Relative permeability curves obtained for the non-fractured micromodel in water fraction flow rate (f_w) ranging from 1 to 0.1.

At $f_w = 1$, only water is injected and it displaces oil until reaching a remaining oil saturation of $S_{or} = 0.16$, which corresponded to $S_w = 0.84$. The residual oil saturation in this test was much lower than that observed during the previous test in which the fw increased. The initial water saturation was also higher in this test, close to $S_{wi} = 0.27$. The relative permeability curves followed the expected behavior, with a decrease in the relative permeability of water and an increase in that of oil as the water saturation decreased.

Tables 4.2 and 4.3 present the results of relative permeability tests conducted on fractured micromodels during the increase water fraction flow rate ($f_w = 0.1$ to 1) and the decrease water fraction flow rate process ($f_w = 1$ to 0.1).

f_w	S_w	ΔP (Pa)	Kr_w	Kr_o
0.1	0.17	11045	0.002	0.434
0.2	0.21	18894	0.003	0.360
0.3	0.21	20232	0.006	0.365
0.4	0.24	17458	0.009	0.376
0.5	0.25	14544	0.012	0.338
0.6	0.30	13462	0.016	0.297
0.7	0.32	12242	0.022	0.253
0.8	0.32	10808	0.031	0.209
0.9	0.33	8694	0.053	0.160
1	0.52	5691	0.153	0

f_w	S_w	ΔP (Pa)	Kr_w	Kr_o
1	0.27	1224	0.325	0
0.9	0.30	4156	0.086	0.209
0.8	0.31	6142	0.052	0.283
0.7	0.31	8084	0.035	0.323
0.6	0.32	10138	0.024	0.343
0.5	0.37	13843	0.014	0.314
0.4	0.39	15975	0.010	0.326
0.3	0.40	17688	0.007	0.344
0.2	0.41	19487	0.004	0.357
0.1	0.40	17960	0.002	0.436

Table 4.2: Fractured micromodel Z1 data sets obtained from relative permeability tests.

f_w	S_w	ΔP (Pa)	Kr_w	Kr_o
0.1	0.03	8829	0.003	0.765
0.2	0.04	8351	0.007	0.719
0.3	0.05	7745	0.011	0.678
0.4	0.05	7207	0.015	0.624
0.5	0.07	7000	0.020	0.536
0.6	0.08	5996	0.028	0.500
0.7	0.11	5510	0.035	0.408
0.8	0.13	4722	0.047	0.318
0.9	0.16	3311	0.075	0.227
1	0.32	1391	0.199	0

f_w	S_w	ΔP (Pa)	Kr_w	Kr_o
1	0.56	1374	0.213	0
0.9	0.31	4045	0.065	0.196
0.8	0.26	4970	0.047	0.320
0.7	0.34	8924	0.023	0.267
0.6	0.36	11382	0.015	0.279
0.5	0.33	10556	0.014	0.376
0.4	0.33	12521	0.009	0.381
0.3	0.33	12238	0.007	0.454
0.2	0.34	12967	0.005	0.490
0.1	0.35	13151	0.002	0.544

Table 4.3: Fractured micromodel L2 data sets obtained from relative permeability tests.

According the data, in both fractured micromodels, a decrease in water injection leads to a reduction in the relative permeability of the water phase and a corresponding increase in the oil permeability - a behavior that aligns with expectations. In the L2 fractured micromodel, water saturation in the porous matrix displayed a non-monotonic trend. In the Z1 fractured micromodel, an even more unexpected behavior was observed: water saturation increased from $S_w = 0.27$ at $f_w = 1$ to $S_w = 0.40$ at $f_w = 0.1$, despite the decreasing water injection. This counterintuitive behavior in saturation was consistently observed across three independent experiments. The physical mechanisms driving this phenomenon remain unclear and are currently under investigation. Possible contributing factors include increased pressure in the porous medium resulting from higher oil injection rates, flow instabilities, pore-scale trapping effects, or other dynamic interactions within the fractured structure.

5
Final Remarks

This study presented an experimental investigation of two-phase flow in fractured porous media, focusing on determining relative permeability curves using PDMS/glass microfluidic micromodels. The experiments demonstrated that heterogeneous porous media, particularly those containing fractures, exhibit markedly different flow behavior compared to homogeneous systems. By applying Darcy's law, both absolute permeabilities and relative permeability curves were obtained, allowing for a detailed evaluation of how structural heterogeneity influences flow dynamics.

The comparison between a homogeneous porous matrix and fractured media highlighted the impact of fractures on two-phase flow. Fractures acted as preferential flow paths, facilitating early water breakthrough due to their low resistance to flow, especially in systems with predominantly oil-wet characteristics. This early breakthrough led to reduced oil recovery and increased fluids trapping within the porous matrix.

Furthermore, the results indicated that fractures directly influence the initial saturation conditions and are closely associated with the occurrence of hysteresis in the relative permeability curves. Variations in fracture geometry and orientation, along with interactions between the fluid phases, led to the formation of distinct flow structures that significantly affected the shape and behavior of the resulting curves. These findings reinforce the notion that relative permeability is not determined solely by saturation but instead arises from a complex interplay of multiple factors, including fluid properties, porous medium geometry, fracture flow patterns, and initial system conditions.

Overall, the results emphasize the importance of accounting for structural heterogeneity when assessing two-phase flow in fractured porous media. Fractures play a key role in controlling saturation dynamics, displacement efficiency, and the overall hydraulic behavior of the medium.

The use of microfluidic micromodels proved to be an effective approach for studying pore-scale interactions, while also contributing to the refinement of more controlled experimental techniques. These experimental advancements, when integrated with established methodologies, support the development of more representative and accurate predictive models for reservoir engineering applications.

Future research should further explore the effects of wettability, injection rates, fluid properties, and transient flow regimes, particularly in systems with more complex fracture geometries featuring diverse orientations, shapes, and degrees of connectivity. Incorporating these variables will help to deepen the understanding of two-phase flow mechanisms in highly heterogeneous fractured systems, supporting the development of predictive models that are more robust and representative of field conditions.

Bibliography

1 LENORMAND, R. Liquids in porous media. **Journal of Physics: Condensed Matter**, IOP Publishing, v. 2, n. S, p. SA79, 1990.

2 JOEKAR-NIASAR, V.; HASSANIZADEH, S. Analysis of fundamentals of two-phase flow in porous media using dynamic pore-network models: A review. **Critical reviews in environmental science and technology**, Taylor & Francis, v. 42, n. 18, p. 1895–1976, 2012.

3 SHAD, S.; MAINI, B. B.; GATES, I. D. Effect of fracture and flow orientation on two-phase flow in an oil-wet fracture: Relative permeability curves and flow structures. In: SPE. **SPE Western Regional Meeting**. [S.l.], 2010. p. SPE–132229.

4 WARREN, J. E.; ROOT, P. J. The behavior of naturally fractured reservoirs. **Society of Petroleum Engineers Journal**, SPE, v. 3, n. 03, p. 245–255, 1963.

5 MOHAMMED, I. et al. A review of pressure transient analysis in reservoirs with natural fractures, vugs and/or caves. **Petroleum Science**, Springer, v. 18, p. 154–172, 2021.

6 HEINEMANN, Z.; MITTERMEIR, G. Fluid flow in porous media. PHDG, 2013.

7 GOLPARVAR, A. et al. A comprehensive review of pore scale modeling methodologies for multiphase flow in porous media. **Advances in Geo-Energy Research**, Yandy Scientific Press, v. 2, n. 4, p. 418–440, 2018.

8 SINGH, K. et al. Dynamics of snap-off and pore-filling events during two-phase fluid flow in permeable media. **Scientific reports**, Nature Publishing Group UK London, v. 7, n. 1, p. 5192, 2017.

9 HUA, W. et al. Research progress of carbon capture and storage (ccs) technology based on the shipping industry. **Ocean Engineering**, Elsevier, v. 281, p. 114929, 2023.

10 MERLISS, F.; DOANE, J.; RZASA, M. Influence of rock and fluid properties on immiscible fluid-flow behavior in porous media. In: SPE. **SPE Annual Technical Conference and Exhibition?** [S.l.], 1955. p. SPE–510.

11 ESCALANTE, J. D. F. Jesus daniel fernandez escalante relative permeability measurement and two-phase flow visualization in micromodels of vugular porous media. In: . [s.n.], 2023. Disponível em: <https://api.semanticscholar.org/CorpusID:261860102>.

12 BERRE, I.; DOSTER, F.; KEILEGAVLEN, E. Flow in fractured porous media: A review of conceptual models and discretization approaches. **Transport in Porous Media**, Springer, v. 130, n. 1, p. 215–236, 2019.

13 BROWN, G. Henry darcy and the making of a law. **Water Resources Research**, Wiley Online Library, v. 38, n. 7, p. 11–1, 2002.

14 HONARPOUR, M.; MAHMOOD, S. Relative-permeability measurements: An overview. **Journal of petroleum technology**, SPE, v. 40, n. 08, p. 963–966, 1988.

15 XU, P. et al. Prediction of relative permeability in unsaturated porous media with a fractal approach. **International Journal of Heat and Mass Transfer**, Elsevier, v. 64, p. 829–837, 2013.

16 GUNDA, N. S. K. et al. Reservoir-on-a-chip (roc): A new paradigm in reservoir engineering. **Lab on a Chip**, Royal Society of Chemistry, v. 11, n. 22, p. 3785–3792, 2011.

17 AMORIM, C. de. **Pore-Scale Mechanisms of Oil Displacement by Emulsion Injection**. Tese (Doutorado) — PUC-Rio, 2024.

18 ENGELKE, B. S. Determinação das curvas de permeabilidade relativa no escoamento de emulsões e óleo. **Rio de Janeiro**, 2012.

19 FERNANDO, S. V.; LEY, H. C. et al. Fluid flow through carbonate rock systems. In: **Developments in petroleum science**. [S.l.]: Elsevier, 1992. v. 30, p. 439–503.

20 ROSA, A. J.; CARVALHO, R. de S.; XAVIER, J. A. D. **Engenharia de reservatórios de petróleo**. [S.l.]: Interciência, 2006.

21 COLLINS, R. E. **Flow of fluids through porous materials**. Petroleum Publishing Co.,Tulsa, OK, 1976. Disponível em: <https://www.osti.gov/biblio/7099752>.

22 MOHAMADI-BAGHMOLAEI, M. et al. Novel method for estimation of gas/oil relative permeabilities. **Journal of Molecular Liquids**, Elsevier, v. 223, p. 1185–1191, 2016.

23 ALI, J. Developments in measurement and interpretation techniques in coreflood tests to determine relative permeabilities. In: SPE. **SPE Latin America and Caribbean Petroleum Engineering Conference**. [S.l.], 1997. p. SPE–39016.

24 SANDBERG, C.; GOURNAY, L.; SIPPEL, R. The effect of fluid-flow rate and viscosity on laboratory determinations of oil-water relative permeabilities. **Transactions of the AIME**, SPE, v. 213, n. 01, p. 36–43, 1958.

25 SCHEMBRE, J.; KOVSCEK, A. A technique for measuring two-phase relative permeability in porous media via x-ray ct measurements. **Journal of Petroleum Science and Engineering**, Elsevier, v. 39, n. 1-2, p. 159–174, 2003.

26 ALYAFEI, N.; AL-MENHALI, A.; BLUNT, M. J. Experimental and analytical investigation of spontaneous imbibition in water-wet carbonates. **Transport in Porous Media**, Springer, v. 115, p. 189–207, 2016.

27 WANG, Z. et al. Experimental and theoretical determination of relative permeability together with microscopic remaining oil distribution based on pore-throat structures. **Geoenergy Science and Engineering**, Elsevier, v. 247, p. 213630, 2025.

28 RANGEL-GERMAN, E.; AKIN, S.; CASTANIER, L. Multiphase-flow properties of fractured porous media. In: SPE. **SPE Western Regional Meeting**. [S.l.], 1999. p. SPE–54591.

29 AKIN, S. Estimation of fracture relative permeabilities from unsteady state corefloods. **Journal of Petroleum Science and Engineering**, Elsevier, v. 30, n. 1, p. 1–14, 2001.

30 LIAN, P.; CHENG, L. The characteristics of relative permeability curves in naturally fractured carbonate reservoirs. **Journal of Canadian Petroleum Technology**, SPE, v. 51, n. 02, p. 137–142, 2012.

31 VILHENA, O. et al. Experimental and numerical evaluation of spontaneous imbibition processes in unfractured and fractured carbonate cores with stress-induced apertures. In: SPE. **SPE Europec featured at EAGE Conference and Exhibition?** [S.l.], 2019. p. D041S010R004.

32 TSAKIROGLOU, C. et al. Experimental study of the immiscible displacement of shear-thinning fluids in pore networks. **Journal of colloid and interface science**, Elsevier, v. 267, n. 1, p. 217–232, 2003.

33 GOGOI, S.; GOGOI, S. B. Review on microfluidic studies for eor application. **Journal of Petroleum Exploration and Production Technology**, Springer, v. 9, p. 2263–2277, 2019.

34 PERSOFF, P.; PRUESS, K. Two-phase flow visualization and relative permeability measurement in natural rough-walled rock fractures. **Water resources research**, Wiley Online Library, v. 31, n. 5, p. 1175–1186, 1995.

35 FOURAR, M. et al. Two-phase flow in smooth and rough fractures: Measurement and correlation by porous-medium and pipe flow models. **Water Resources Research**, Wiley Online Library, v. 29, n. 11, p. 3699–3708, 1993.

36 DIOMAMPO, G. P. et al. Relative permeability through fractures. In: **Proc. 27 the Workshop on Geothermal Reservoir Engineering**. [S.l.: s.n.], 2001. p. 28–30.

37 FAHAD, M. et al. Experimental investigation of upscaling relative permeability for two phase flow in fractured porous media. **Journal of Petroleum Science and Engineering**, Elsevier, v. 149, p. 367–382, 2017.

38 AVENDAÑO, J. et al. Effect of surface wettability on immiscible displacement in a microfluidic porous media. **Energies**, MDPI, v. 12, n. 4, p. 664, 2019.

39 KENZHEKHANOV, S. **Chemical EOR process visualization using NOA81 micromodels**. [S.l.]: Colorado School of Mines, 2016.

40 HUSSAIN, S. T. et al. Multiphase fluid flow through fractured porous media supported by innovative laboratory and numerical methods for estimating relative permeability. **Energy & Fuels**, ACS Publications, v. 35, n. 21, p. 17372–17388, 2021.

41 WU, M. et al. Single-and two-phase flow in microfluidic porous media analogs based on voronoi tessellation. **Lab on a Chip**, Royal Society of Chemistry, v. 12, n. 2, p. 253–261, 2012.

42 XU, W. et al. Effect of pore geometry and interfacial tension on water-oil displacement efficiency in oil-wet microfluidic porous media analogs. **Physics of Fluids**, AIP Publishing, v. 26, n. 9, 2014.

43 SABOORIAN-JOOYBARI, H. Analytical estimation of water-oil relative permeabilities through fractures. **Oil & Gas Science and Technology–Revue d'IFP Energies nouvelles**, EDP Sciences, v. 71, n. 3, p. 31, 2016.

44 ROMM, E. Flow characteristics of fractured rocks. **Nedra, Moscow**, v. 283, 1966.

45 PAN, X. **Immiscible two-phase flow in a fracture**. [S.l.]: National Library of Canada= Bibliotheque nationale du Canada, Ottawa, 2001.

46 BARENBLATT, G. I.; ZHELTOV, I. P.; KOCHINA, I. Basic concepts in the theory of seepage of homogeneous liquids in fissured rocks [strata]. **Journal of applied mathematics and mechanics**, Pergamon, v. 24, n. 5, p. 1286–1303, 1960.

47 PRUESS, K.; TSANG, Y. On two-phase relative permeability and capillary pressure of rough-walled rock fractures. **Water resources research**, Wiley Online Library, v. 26, n. 9, p. 1915–1926, 1990.

48 FOURAR, M.; LENORMAND, R. A viscous coupling model for relative permeabilities in fractures. In: SPE. **SPE Annual Technical Conference and Exhibition?** [S.l.], 1998. p. SPE–49006.

49 WATANABE, N. et al. New ν-type relative permeability curves for two-phase flows through subsurface fractures. **Water Resources Research**, Wiley Online Library, v. 51, n. 4, p. 2807–2824, 2015.

50 YE, Z. et al. Two-phase flow properties in aperture-based fractures under normal deformation conditions: Analytical approach and numerical simulation. **Journal of Hydrology**, Elsevier, v. 545, p. 72–87, 2017.

51 HATAMI, S.; WALSH, S. D. Relative permeability of two-phase flow through rough-walled fractures: Effect of fracture morphology and flow dynamics. **Journal of Hydrology**, Elsevier, v. 613, p. 128326, 2022.

52 XIA, Y.; WHITESIDES, G. M. Soft lithography. **Annual review of materials science**, Annual Reviews 4139 El Camino Way, PO Box 10139, Palo Alto, CA 94303-0139, USA, v. 28, n. 1, p. 153–184, 1998.

53 BHATTACHARYA, S. et al. Studies on surface wettability of poly (dimethyl) siloxane (pdms) and glass under oxygen-plasma treatment and correlation with bond strength. **Journal of microelectromechanical systems**, IEEE, v. 14, n. 3, p. 590–597, 2005.

54 TAN, S. H. et al. Oxygen plasma treatment for reducing hydrophobicity of a sealed polydimethylsiloxane microchannel. **Biomicrofluidics**, American Institute of Physics, v. 4, n. 3, p. 032204, 2010.

55 CHEN, C.-Y.; HORNE, R. N.; FOURAR, M. Experimental study of liquid-gas flow structure effects on relative permeabilities in a fracture. **Water resources research**, Wiley Online Library, v. 40, n. 8, 2004.

56 WONG, R.-K.; PAN, X.; MAINI, B. Correlation between pressure gradient and phase saturation for oil-water flow in smooth-and rough-walled parallel-plate models. **Water Resources Research**, Wiley Online Library, v. 44, n. 2, 2008.

A
Appendice

A.1
Example of macro script used for image processing

The following macro script was developed in Fiji to automate the image pre-processing and analysis steps described in this work.

```
sourceDir = "Documents/Experiments/Images/Merges/";

list_imgs = getFileList(sourceDir);
for (i = 0; i < list_imgs.length; i++)
{

 save_imgs = sourceDir + "Merges_processed/";
 File.makeDirectory(save_imgs);

 open(sourceDir + list_imgs[i]);

 //crop and rotate
 run("Rotate... ", "angle=2.5 grid=1 interpolation=Bilinear");
 run("Flip Horizontally");
 //setTool("rectangle");
 makeRectangle(2112, 553, 19452, 4856);  //crop only the porous medium
 run("Crop");

 //run("Brightness/Contrast...");
 setMinAndMax(-95, 159);
 run("8-bit");
 //run("Threshold...");
 setAutoThreshold("Otsu dark no-reset");
 //setThreshold(219, 255);
 setOption("BlackBackground", true);
 run("Convert to Mask");
 run("Remove Outliers...", "radius=7.5 threshold=50 which=Dark");
```

```
 run("Invert");
 run("Analyze Particles...", "display summarize");
 saveAs("Tiff", save_imgs + list_imgs[i] + "_processed");
 close("*");

}

  if (isOpen("Summary") && isOpen("Results"))
      {

      selectWindow("Summary");
      saveAs("Results", save_imgs + "Summary.csv");
      run("Close");
      selectWindow("Results");
      saveAs("Results", save_imgs + "Results.csv");
      run("Close");

      }
```